OPTIMAL DEFINITION OF THE NONLINEAR WEIGHTS IN MULTIDIMENSIONAL CENTRAL WENOZ RECONSTRUCTIONS*

I. CRAVERO†, M. SEMPLICE†, AND G. VISCONTI‡

Abstract. Central WENO reconstruction procedures have shown very good performance in finite volume and finite difference schemes for hyperbolic conservation and balance laws in one and higher space dimensions on different types of meshes. Their most recent formulations include WENOZ-type nonlinear weights, but in this context a thorough analysis of the global smoothness indicator τ is still lacking. In this work we first prove results on the asymptotic expansion of one- and multidimensional Jiang–Shu smoothness indicators that are useful for the rigorous design of CWENOZ schemes, which are in addition to those considered in this paper. Next, we introduce the optimal definition of τ for the one-dimensional CWENOZ schemes and for one example of two-dimensional CWENOZ reconstruction. Numerical experiments of one- and two-dimensional test problems show the correctness of the analysis and the good performance of the new schemes.

Key words. central WENOZ (CWENOZ), essentially nonoscillatory reconstructions, finite volume schemes, smoothness indicators

AMS subject classifications. 65M08, 65M20

DOI. 10.1137/18M1228232

1. Introduction. In this paper we focus on point-value reconstruction from cell averages employed in multidimensional finite volume schemes for the numerical approximation of the solutions of systems of hyperbolic balance laws of the form

$$\text{(1)} \qquad \partial_t \mathbf{u} + \nabla_{\mathbf{x}} \cdot \mathbf{f}(\mathbf{u}) = \mathbf{s}(\mathbf{u}).$$

Here $\mathbf{u} = \mathbf{u}(t, \mathbf{x}) : \mathbb{R}^+ \times \mathbb{R}^n \to \mathbb{R}^J$ is the unknown describing the physical states, n is the number of space dimensions, and J is the number of equations. The vector valued function $\mathbf{f}(\mathbf{u})$ is the flux and is a smooth known function of $\mathbf{u}$, whose Jacobian is assumed diagonalizable with real eigenvalues along all possible directions in $\mathbb{R}^n$ in order to guarantee that (1) is a hyperbolic system. Finally, the vector valued function $\mathbf{s}(\mathbf{u})$ is the source term. We assume that (1) is set in a bounded domain $\mathcal{D} \subset \mathbb{R}^n$ and is complemented by appropriate initial and boundary conditions on $\partial\mathcal{D}$.

Finite volume methods partition the domain $\mathcal{D}$ into cells $\Omega_j \subset \mathbb{R}^n$ such that $\mathcal{D} = \cup_j \Omega_j$, where $\Omega_i \cap \Omega_j \subset \partial\Omega_i$ for any $i \neq j$. The time evolution of the solution is computed by solving the system of ordinary differential equations (ODEs)

$$\text{(2)} \qquad \frac{\mathrm{d}\overline{\mathbf{u}}_j}{\mathrm{d}t} = -\frac{1}{|\Omega_j|} \int_{\partial\Omega_j} \mathbf{f}(\mathbf{u}(t, \gamma)) \cdot \mathbf{n}(\gamma)\mathrm{d}\gamma + \frac{1}{|\Omega_j|} \int_{\Omega_j} \mathbf{s}(\mathbf{u}(t, \mathbf{x}))\mathrm{d}\mathbf{x}$$

for the cell averages

$$\text{(3)} \qquad \overline{\mathbf{u}}_j(t) = \frac{1}{|\Omega_j|} \int_{\Omega_j} \mathbf{u}(t, \mathbf{x})\mathrm{d}\mathbf{x},$$

†Dipartimento di Matematica, Università di Torino, 10123 Torino, Italy (isabella.cravero@unito.it, matteo.semplice@unito.it).
‡RWTH Aachen University, 52062 Aachen, Germany (visconti@igpm.rwth-aachen.de).

where $\partial \Omega_j$ is the cell boundary, $|\Omega_j|$ is the volume of Ω_j, and $\mathbf{n}$ is the outward unit normal to $\partial \Omega_j$. In order to compute the right-hand side of (2), we need point values of $\mathbf{u}$ at the cell boundary (and inside the cell if $\mathbf{s} \neq \mathbf{0}$). Since only the cell averages are stored, such values are approximated by a so-called reconstruction procedure, which computes a function $\mathbf{R}_j(\mathbf{x})$ that approximates the unknown function $\mathbf{u}(\mathbf{x})$ in the cell Ω_j with a chosen accuracy $G + 1$. In particular, such reconstructions are needed at the nodes of the quadrature rules used to compute the integrals in (2). For example, a third order scheme in two space dimensions would require at least eight nodes for the boundary term and four extra inner nodes for the source.

It is well known that defining $\mathbf{R}_j(\mathbf{x})$ as a polynomial interpolant on a fixed stencil yields oscillatory results in any high order scheme. The most popular reconstruction procedure for accuracy greater than two is surely the Weighted Essentially Nonoscillatory (WENO) reconstruction [27, 38], which reconstructs point values as a convex combination of point values of low-degree interpolants. The coefficients of the combination, the *nonlinear weights*, depend nonlinearly on the data and are designed to reproduce, at a specific point, the value of a high-degree central interpolant in smooth areas and to provide a lower accuracy but nonoscillatory reconstruction elsewhere. The whole construction depends on the existence and positivity of a set of *linear* or *optimal weights*.

The WENO linear weights are thus fixed by accuracy requirements and depend on the location of the reconstruction point and on the size and relative location of the neighboring cells. The computation of nonlinear weights must then be repeated for each reconstruction point. Moreover, even in one space dimension, the existence (and positivity) of the linear weights is not guaranteed for a generic point in Ω_j [33].

Attempts to extend the definition of WENO to non-Cartesian meshes had to tackle the formidable task of computing the linear weights for very general cell arrangements, and most authors chose either to follow the original philosophy of using only low order polynomials but very complex computations of the optimal linear weights for each reconstruction point [25, 36, 44], or to employ a central high order polynomial with low order directionally biased ones [4, 19, 40].

We point out that the older ENO approach [23], which simply selects a reconstruction polynomial from among a set of candidates, does not depend on point- or accuracy-dependent quantities, and additionally provides a polynomial that is defined and uniformly accurate in the whole cell. However, the stencil of an ENO reconstruction is much wider that the stencil of a WENO one of the same order.

The Central WENO (CWENO) reconstruction, first introduced by Levy, Puppo, and Russo in the one-dimensional context [30], enjoys the benefits of both ENO and WENO but but none of their drawbacks. In fact, CWENO makes use of linear weights that can be fixed independently of the reconstruction point, since they need not satisfy accuracy requirements. As a consequence, CWENO, unlike WENO, does not suffer from existence and positivity issues of the weights and, moreover, like ENO it yields a reconstruction polynomial for the entire cell. The nonlinear weights are then computed by a nonlinear procedure similar to the WENO one but applied only once per cell and not once per reconstruction point. This is particularly advantageous for very high order schemes, given the high number of flux quadrature points, and even more for balance laws, due to the additional source term quadrature (see, e.g., [6]).

After the seminal paper [30], the one-dimensional CWENO technique was extended to fifth order [10], and the properties of the third order versions were studied in detail on uniform [28] and nonuniform meshes [15]. Finally, arbitrary high order variants were introduced [14], where the class of CWENO reconstructions was defined. The Adaptive Order WENO (WAO) of [3] also belongs to this class.

To extend the CWENO procedure to more than one space dimension, [31] combined a bivariate central parabola and four linear polynomials. In a similar fashion, [34] obtained a third order accurate reconstruction on two-dimensional quad-tree meshes. Other approaches exploit a combination of central polynomials defined in each neighbor [32, 29] or a combination of polynomials, each of which can be of degree one or two [21]. More recently, in the context of finite volume P_0P_M schemes [17, 18] combined high- and low-degree polynomials to obtain an arbitrary high order CWENO construction for triangular and tetrahedral meshes. Later, this idea was also exploited in the subcell limiter for a discontinuous Galerkin scheme [7].

An alternative definition of the WENO nonlinear weights was given in [5] and further developed in [11, 16], resulting in the WENOZ reconstruction procedure. The nonlinear weights of WENOZ are based on an additional global smoothness indicator τ which is a linear combination of the WENO indicators. A similar definition of the nonlinear weights was employed in the CWENO context as well, resulting in the so-called CWENOZ schemes. Schemes of this class are presented in [13, 43, 45, 46], although sometimes under different names. The paper [13] compares the WENOZ and CWENOZ reconstructions with WENO and CWENO, finding that the former have better spectral properties. Note that in [1] a further technique for computing the nonlinear weights was introduced that still relies on the WENOZ idea and introduces an additional indicator.

In this paper we focus on the optimization and generalization of the CWENOZ reconstruction of [13] to higher space dimensions, without relying on dimensional splitting, in the same spirit as [34]. A very important contribution of this paper is a set of theoretical results that give sufficient conditions for a CWENOZ reconstruction to be of an optimal order of accuracy. This is discussed and enriched by many examples in section 2, where some useful results on the Taylor expansion of Jiang–Shu indicators in one and higher space dimensions are also proved.

In section 3, we build on the previous results to derive a new and optimal definition of the τ parameter of the one- and two-dimensional CWENOZ reconstructions tested in this paper. Section 4 contains the numerical tests for the accuracy of the reconstructions and on their application to semidiscrete finite volume schemes for systems of conservation laws in one and two space dimensions. Finally, section 5 summarizes the findings of this paper. Alongside this article we provide supplementary material, in particular a PDF document containing the explicit expression of the quantities involved in the results of section 2 in some well-known cases, and some additional details about the setup of the numerical experiments of section 4. Citations beginning with "SM" point to this document. Also, movies for some numerical tests are provided in the supplementary material.

2. Analysis of n-dimensional CWENO and CWENOZ reconstructions. In this section we prove the theoretical results for analyzing the CWENO and CWENOZ reconstruction procedures in one and higher space dimensions. To this end, we restrict our attention to the scalar case since, usually, in the case of systems of conservation laws, the reconstruction procedures are applied componentwise, directly to the conserved variables or after the local characteristic projection.

We consider a Cartesian grid in n space dimensions, composed of a union of rectangular cells $\Omega_k \subset \mathbb{R}^n$ of dimension $\boldsymbol{\Delta}\mathbf{x} \in \mathbb{R}^n$ and diameter $\rho := \|\boldsymbol{\Delta}\mathbf{x}\|_2$.

2.1. Definition and examples. We recall here the definition of the CWENO and CWENOZ operators, as given in [14] and [13], respectively. Note that the difference between the two methods is in the computation of the nonlinear coefficients: the

CWENOZ method uses the idea of Borges et al. in [5], where they introduced an extra smoothness indicator τ and a new definition of the nonlinear coefficients that drives them closer to their optimal values in the smooth case.

Let $\mathbb{P}_n^k$ be the space of polynomials in n variables with degree at most $k \in \mathbb{N}$.

In order to describe the reconstruction, we consider as given data the cell averages $\overline{u}_k$ of a function u over the cells of a grid. To simplify the notation, we describe the reconstruction of $u(\mathbf{x})$ in the cell Ω_0 centered in the point $\mathbf{x}_0 = \mathbf{0}$ and size $\mathbf{\Delta x} \in \mathbb{R}^n$.

DEFINITION 1. *Let $\mathcal{S}$ be a set of η cell indices including 0 (stencil). We associate to $\mathcal{S}$ the polynomial*

$$(4) \quad P_{\mathcal{S}}^{(d)}(\mathbf{x}) = \arg\min\left\{\sum_{i \in \mathcal{S}} \left|\langle P_{\mathcal{S}}^{(d)}\rangle_{\Omega_i} - \overline{u}_i\right|^2, \text{ such that } P_{\mathcal{S}}^{(d)} \in \mathbb{P}_n^d, \langle P_{\mathcal{S}}^{(d)}\rangle_{\Omega_0} = \overline{u}_0\right\},$$

where the operator $\langle\cdot\rangle_{\Omega_i}$ denotes the cell average of its argument over the cell Ω_i. Of course η should be larger than the number of coefficients in $P_{\mathcal{S}}^{(d)}$.

Remark 2. If the number of coefficients in $P_{\mathcal{S}}^{(d)}(\mathbf{x})$ is equal to η, the constrained least squares polynomial $P_{\mathcal{S}}^{(d)}(\mathbf{x})$ is the ordinary polynomial interpolating the given cell averages of the stencil $\mathcal{S}$ exactly. We observe, as in [34], that if (4) is overdetermined and full rank, it suffices to choose a basis such that $\langle\varphi_k\rangle_{\Omega_0} = 0$ and express

$$P_{\mathcal{S}}^{(d)}(\mathbf{x}) = \overline{u}_0 + \sum_k c_k \varphi_k(\mathbf{x})$$

in order to turn (4) into an unconstrained least squares problem for the coefficients c_k with right-hand sides $\overline{u}_k - \overline{u}_0$. The existence of a unique least squares polynomial $P_{\mathcal{S}}^{(d)}(\mathbf{x})$ is guaranteed by the convexity of the problem defined in (4).

The nonlinear selection or blending of polynomials taking place in any ENO reconstruction relies on *oscillation indicators*. In general, these are scalar quantities $I[P]$ associated to a polynomial P that are designed in such a way that $I[P] \to 0$ under grid refinement if P is associated to smooth data. Moreover, $I[P]$ is in all cases a bounded quantity, even if a discontinuity is present in the stencil of P; in this latter case, it is desirable that $I[P] \asymp 1$. The Jiang–Shu indicators defined in [27] are the most widely used (see Definition 11).

We are now in position to define the CWENO and CWENOZ reconstructions.

DEFINITION 3. *Given a stencil $\mathcal{S}_{\mathsf{opt}}$ that includes the cell Ω_0, let $P_{\mathsf{opt}} \in \mathbb{P}_n^G$ (optimal polynomial) be the polynomial of degree G associated to $\mathcal{S}_{\mathsf{opt}}$. Further, let $P_1, P_2, \ldots, P_m$ be a set of $m \geq 1$ polynomials of degree g with $g < G$ associated to substencils such that $0 \in \mathcal{S}_k \subset \mathcal{S}_{\mathsf{opt}}$. Let also $\{d_k\}_{k=0}^m$ be a set of strictly positive real coefficients such that $\sum_{k=0}^m d_k = 1$.*

The CWENO and CWENOZ operators compute a reconstruction polynomial

$$P_{\mathsf{rec}}^{CW} = \mathsf{CWENO}(P_{\mathsf{opt}}, P_1, \ldots, P_m) \in \mathbb{P}_n^G,$$
$$P_{\mathsf{rec}}^{CWZ} = \mathsf{CWENOZ}(P_{\mathsf{opt}}, P_1, \ldots, P_m) \in \mathbb{P}_n^G$$

as follows:

1. *First, introduce the polynomial P_0 defined as*

$$(5) \qquad P_0(\mathbf{x}) = \frac{1}{d_0}\left(P_{\mathsf{opt}}(\mathbf{x}) - \sum_{k=1}^m d_k P_k(\mathbf{x})\right) \in \mathbb{P}_n^G;$$

2. *compute suitable regularity indicators*

$$I_0 = I[P_{\mathsf{opt}}], \qquad I_k = I[P_k], \ k \geq 1;$$

3. *compute the nonlinear coefficients* $\{\omega_k\}_{k=0}^m$ *or* $\{\omega_k^Z\}_{k=0}^m$ *as*
   (3.i) CWENO *operator: for* $k = 0, \ldots, m,$

$$(6a) \qquad \alpha_k = \frac{d_k}{(I_k + \epsilon)^\ell}, \qquad \omega_k^{\mathsf{CW}} = \frac{\alpha_k}{\sum_{i=0}^m \alpha_i},$$

   (3.ii) CWENOZ *operator: for* $k = 0, \ldots, m,$

$$(6b) \qquad \alpha_k^Z = d_k \left(1 + \left(\frac{\tau}{I_k + \epsilon} \right)^\ell \right), \qquad \omega_k^{\mathsf{CWZ}} = \frac{\alpha_k^Z}{\sum_{i=0}^m \alpha_i^Z},$$

   where ϵ *is a small positive quantity,* $\ell \geq 1$, *and, in the case of* CWENOZ, τ
   is a global smoothness indicator; and

4. *finally, define the reconstruction polynomial as*

$$(7a) \qquad P_{\mathsf{rec}}^{CW}(\mathbf{x}) = \sum_{k=0}^m \omega_k^{\mathsf{CW}} P_k(\mathbf{x}) \in \mathbb{P}_n^G,$$

$$(7b) \qquad P_{\mathsf{rec}}^{CWZ}(\mathbf{x}) = \sum_{k=0}^m \omega_k^{\mathsf{CWZ}} P_k(\mathbf{x}) \in \mathbb{P}_n^G.$$

This extends the definitions given in [14, 13]. We point out that the use of equation (5) is what characterizes a central WENO reconstruction and that both WENO-ZQ [45] and WAO [3] in fact belong to this class.

Note that the reconstruction polynomial defined in (7) can be evaluated at any reconstruction point in the computational cell at a very low computational cost, since the coefficients of P_{rec} can be computed with (7) in any convenient basis for $\mathbb{P}_n^G$. It is important to note that the linear coefficients $\{d_k\}_{k=0}^m$ do not depend on the reconstruction point, and thus the nonlinear coefficients (6a) and (6b) can be computed once per cell and not once per reconstruction point, as in the standard WENO. This makes the CWENO idea less computationally expensive than the WENO procedure for balance laws, multidimensional computations, and unstructured meshes.

Remark 4. Thanks to the constraint included in (4), if all the interpolating polynomials involved in Definition 3 are defined by (4), they all satisfy the conservation property on the reconstruction cell Ω_0. Then also the cell average on Ω_0 of P_0, $P_{\mathsf{rec}}^{\mathsf{CW}}$, and $P_{\mathsf{rec}}^{\mathsf{CWZ}}$ is exactly $\bar{u}_0$, and the reconstruction is conservative.

The accuracy and nonoscillatory properties of CWENO and CWENOZ schemes are guaranteed by the dependence of their nonlinear weights (6) on suitable regularity indicators I_k. On smooth data, (6) ought to drive the nonlinear weights sufficiently close to the optimal ones, so that $P_{\mathsf{rec}} \approx P_{\mathsf{opt}}$ and the reconstruction should reach the optimal order of accuracy $G + 1$.

Remark 5. Assume that the stencils are chosen such that the approximation orders of $P_{\mathsf{opt}} \in \mathbb{P}_n^G$ and $P_k \in \mathbb{P}_n^g$, for $k = 1, \ldots, m$, are

$$|P_{\mathsf{opt}}(\mathbf{x}) - u(\mathbf{x})| = \mathcal{O}(\rho^{G+1}) \quad \text{and} \quad |P_k(\mathbf{x}) - u(\mathbf{x})| = \mathcal{O}(\rho^{g+1})$$

at any point $\mathbf{x}$ in the computational cell if the function $u(\mathbf{x})$ is sufficiently regular. Then, using (7) and since $P_{\mathsf{opt}} = \sum_{k=0}^{m} d_k P_k$, the reconstruction error at $\mathbf{x}$ is

$$u(\mathbf{x}) - P_{\mathsf{rec}}(\mathbf{x}) = \underbrace{(u(\mathbf{x}) - P_{\mathsf{opt}}(\mathbf{x}))}_{\mathcal{O}(\rho^{G+1})} + \sum_{k=0}^{m} (d_k - \omega_k) \underbrace{(P_k(\mathbf{x}) - u(\mathbf{x}))}_{\mathcal{O}(\rho^{g+1})},$$

where ω_k and P_{rec} are defined by either (6a) and (7a) or (6b) and (7b). Thus the condition $(d_k - \omega_k) = \mathcal{O}(\rho^{G-g})$ is sufficient to ensure that the accuracy of the CWENO and CWENOZ reconstructions equal the accuracy of its first argument P_{opt} in the case of smooth data.

On the other hand, if there were an oscillating $P_{\hat{k}}$ for some $\hat{k} \in \{1, \ldots, m\}$, then we would have $I_{\hat{k}} \asymp 1$ and $w_{\hat{k}} \approx 0$; moreover, we would also have $w_0 \approx 0$ (see [14]), and P_{rec} would become a nonlinear combination of polynomials of degree g: the accuracy of the reconstruction reduces to $g+1$, but spurious oscillations in the PDE solution would be controlled.

Remark 6. Note that in Definition 3, the regularity indicator I_0 is computed by using the optimal polynomial P_{opt}. In previous works (see, e.g., [13, 14, 15, 34]), I_0 was defined as $I_0 = I[P_0]$. The new definition of I_0 as $I[P_{\mathsf{opt}}]$ simplifies the derivation of an optimal formula for τ and has virtually no ill effects on the accuracy and nonoscillatory properties of the reconstruction (see sections 3.1 and 4.1).

The positive parameter ϵ prevents the division by zero in the computation of the nonlinear weights (6a) and (6b). We would like to choose it as small as possible in order to control spurious oscillations. However, as the authors of [15, 28] proved, the choice of ϵ can influence the convergence of the method on smooth parts of the solution. In [16] it was proved that for WENOZ schemes the condition on ϵ to achieve the optimal order of accuracy is weaker than in standard WENO. In this paper, we also study the lower bound for ϵ in CWENOZ (see section 3 and Table 2).

In view of Remark 5, we point out that the weights of the CWENOZ reconstruction defined in (6b), when compared to (6a) for CWENO, are designed to drive the nonlinear coefficients close to the optimal ones in the case of smooth data: this goal is achieved, as in standard WENOZ schemes [5, 11, 16], by including the additional regularity indicator τ in the computation of the nonlinear weights.

This paper addresses the optimal definition of the extra regularity indicator τ for the CWENOZ scheme, and thus generalizes the results of [16] to the case of central WENO reconstructions and improves the CWENOZ reconstructions of [13].

In Definition 3 the number m and the degree g of the lower-degree polynomials are not specified or linked to the degree G of the optimal polynomial. Here we summarize some traditional choices that have been put forward in the literature.

Example 7 (one dimension of accuracy $2r - 1$). In one space dimension it is customary to choose $g = r - 1$, $m = g + 1$, and P_{opt} of degree $G = 2r - 2$. The latter is determined by the exact interpolation of the data in a symmetric stencil $\mathcal{S}_{\mathrm{opt}}$ centered on Ω_0 containing the cells $\Omega_{-g}, \ldots, \Omega_g$. Furthermore, for $k = 1, \ldots, m$, the lower-degree polynomials P_k are defined as the exact interpolants on the substencils $\mathcal{S}_k = \{k - r, \ldots, k - 1\} \subset \mathcal{S}_{\mathrm{opt}}$. This is the same choice considered in [14, 13].

Example 8 (two dimensions of accuracy 3 on quad-tree grids). In higher space dimensions, [34] considers a CWENO reconstruction of order 3 in which $\mathcal{S}_{\mathrm{opt}}$ is composed by all cells that intersect Ω_0 in a face/edge or vertex in a quad-tree mesh, while $m = 4$ and $\mathcal{S}_k$ are substencils in northeast, northwest, southeast, and southwest

directions. The optimal polynomial is of degree $G = 2$ and is chosen as $P_{\mathsf{opt}} = P_{\mathcal{S}_{\mathsf{opt}}}^{(2)}$, and the four linear polynomials ($g = 1$) are chosen as $P_k = P_{\mathcal{S}_k}^{(1)}$. In [34] it is proved that the aforementioned definitions of the stencils always lead to overdetermined systems in the least squares problem (4) on any possible configuration in a quad-tree mesh. In the same paper, a generalization to octrees in three space dimensions is also suggested.

Example 9 (two and three dimensions of arbitrary accuracy on simplicial meshes). CWENO reconstructions of arbitrary order on simplicial meshes in two and three space dimensions were introduced in [18]. There, a polynomial of degree $G \geq 2$ is combined with $m = 3$ (in two dimensions) or $m = 4$ (in three dimensions) polynomials of degree $g = 1$ in order to enhance the nonoscillatory properties of the schemes. At orders 3 and 4, [46] also presents a similar reconstruction.

Example 10 (two dimensions of order 4 on Cartesian meshes). CWENO reconstructions of order 4 on uniform Cartesian meshes in two space dimensions were introduced in [12]. There, a polynomial of degree $G = 3$ defined by a diamond-shaped central stencil is combined with $m = 4$ polynomials of degree $g = 1$ or $g = 2$.

2.2. Properties of the Jiang–Shu smoothness indicators. We now turn to the study of the accuracy of the CWENOZ reconstructions, but first we need to prove some general properties of the smoothness indicators. The results of this section generalize those of [16] for $n > 1$ and of course specialize to them in the case $n = 1$.

In this section we use the multi-index notation for partial derivatives. In n space dimensions, for a smooth enough function q, we denote, for $\boldsymbol{\alpha} = (\alpha_1, \ldots, \alpha_n) \in \mathbb{N}^n$, $\partial_{\boldsymbol{\alpha}} q := \frac{\partial^{|\boldsymbol{\alpha}|} q}{\partial x_1^{\alpha_1} \ldots \partial x_n^{\alpha_n}}$. Obviously, for $n = 1$, $\partial_{\boldsymbol{\alpha}} q$ denotes an ordinary derivative.

In this paper we employ the multi-dimensional generalization of the classical smoothness indicators defined in [27], which has been employed since [26].

DEFINITION 11. *The smoothness indicator of a polynomial* $q \in \mathbb{P}_n^M$ *is*

$$(8) \qquad I[q] := \sum_{|\boldsymbol{\beta}|=1}^{M} \boldsymbol{\Delta}\mathbf{x}^{2\boldsymbol{\beta}-1} \int_{\Omega_0} (\partial_{\boldsymbol{\beta}} q(\mathbf{x}))^2 \mathrm{d}\mathbf{x}.$$

Here $\mathbf{x}^{\boldsymbol{\alpha}} \in \mathbb{R}$ denotes $\mathbf{x}^{\boldsymbol{\alpha}} := x_1^{\alpha_1} \cdots x_n^{\alpha_n}$. In what follows, we will also use the following notation. For each $k \in \mathbb{N}$, we denote $\boldsymbol{k} := (k, k, \ldots, k)$. For any multi-index $\boldsymbol{\alpha} \in \mathbb{N}^n$, we define $\boldsymbol{\alpha}! := \alpha_1! \cdots \alpha_n!$, $|\boldsymbol{\alpha}| := \sum_{i=1}^{n} \alpha_i$ and $\Pi\boldsymbol{\alpha} := \prod_{i=1}^{n} \alpha_i$. We say that $\boldsymbol{\alpha}$ is even if α_i is even for each $i = 1, \ldots, n$. Finally, we define a partial ordering among multi-indices by $\boldsymbol{\alpha} \leq \boldsymbol{\beta}$ if $\alpha_i \leq \beta_i$ for all $i = 1, \ldots, n$.

In what follows, we will use the notation $\theta(g(\rho)) = r$ to mean that $g(\rho) = a_r \rho^r + o(\rho^r)$ for $\rho \to 0$, with $a_r \neq 0$.

Let $q(\mathbf{x}) = \sum_{|\boldsymbol{\alpha}| \leq M} a_{\boldsymbol{\alpha}} \mathbf{x}^{\boldsymbol{\alpha}}$ be a polynomial of degree M, and let $\mathbf{a} = \{a_{\boldsymbol{\alpha}}\}_{|\boldsymbol{\alpha}| \leq M}$ be the vector of coefficients indexed by $\boldsymbol{\alpha}$.

PROPOSITION 12. *Let* q *be a polynomial in* $\mathbb{P}_n^M$, *and let* $\mathbf{w}(q)$ *be a vector of size* $\dim(\mathbb{P}_n^M) = \binom{M+n}{n}$ *whose components are*

$$(9) \qquad (\mathbf{w}(q))_{\boldsymbol{\alpha}} = \boldsymbol{\Delta}\mathbf{x}^{\boldsymbol{\alpha}} \int_{\Omega_0} \partial_{\boldsymbol{\alpha}} q(\mathbf{x}) \mathrm{d}\mathbf{x} \quad \forall \, \boldsymbol{\alpha} \; s.t. \; |\boldsymbol{\alpha}| = 0, 1, \ldots, M.$$

Then, there exists a square symmetric matrix $\mathbf{A}$ *with constant entries such that*

$$\boldsymbol{\Delta}\mathbf{x}^{\mathbf{1}} \int_{\Omega_0} (q(\mathbf{x}))^2 \mathrm{d}\mathbf{x} = \langle \mathbf{w}(q), \mathbf{A}\mathbf{w}(q) \rangle.$$

Proof. Direct computation shows that

$$(\mathbf{w}(q))_{\boldsymbol{\alpha}} = \boldsymbol{\Delta}\mathbf{x}^{\boldsymbol{\alpha}} \int_{\Omega_0} \partial_{\boldsymbol{\alpha}} q(\mathbf{x}) \mathrm{d}\mathbf{x} = \boldsymbol{\Delta}\mathbf{x}^{\boldsymbol{\alpha}} \sum_{\substack{|\boldsymbol{\beta}| \leq M, \\ \boldsymbol{\beta} \geq \boldsymbol{\alpha}}} a_{\boldsymbol{\beta}} \int_{\Omega_0} \partial_{\boldsymbol{\alpha}} \mathbf{x}^{\boldsymbol{\beta}} \mathrm{d}\mathbf{x}.$$

The integral terms are nonzero only if $\boldsymbol{\beta} - \boldsymbol{\alpha}$ is even and they are equal to

$$\int_{\Omega_0} \partial_{\boldsymbol{\alpha}} \mathbf{x}^{\boldsymbol{\beta}} \mathrm{d}\mathbf{x} = \frac{\boldsymbol{\beta}!}{(\boldsymbol{\beta} - \boldsymbol{\alpha})!} \int_{\Omega_0} \mathbf{x}^{\boldsymbol{\beta} - \boldsymbol{\alpha}} \mathrm{d}\mathbf{x} = \frac{\boldsymbol{\beta}! \, \boldsymbol{\Delta}\mathbf{x}^{\boldsymbol{\beta} - \boldsymbol{\alpha} + 1}}{2^{|\boldsymbol{\beta} - \boldsymbol{\alpha}|}(\boldsymbol{\beta} - \boldsymbol{\alpha} + 1)!}.$$

Thus,

$$(\mathbf{w}(q))_{\boldsymbol{\alpha}} = \sum_{\substack{|\boldsymbol{\beta}| \leq M, \boldsymbol{\beta} \geq \boldsymbol{\alpha}, \\ \boldsymbol{\beta} - \boldsymbol{\alpha} \text{ even}}} a_{\boldsymbol{\beta}} \frac{\boldsymbol{\beta}!}{(\boldsymbol{\beta} - \boldsymbol{\alpha} + 1)! \, 2^{|\boldsymbol{\beta} - \boldsymbol{\alpha}|}} \boldsymbol{\Delta}\mathbf{x}^{\boldsymbol{\beta} + 1}$$

or, in matrix form,

$$\mathbf{w}(q) = \mathbf{U}\,\mathbf{D}\,\mathbf{a},$$

where $\mathbf{D}$ is a diagonal matrix $\mathbf{D}_{\boldsymbol{\alpha},\boldsymbol{\alpha}} = \boldsymbol{\Delta}\mathbf{x}^{\boldsymbol{\alpha}+1}$ and $\mathbf{U}$ is an upper triangular constant matrix whose elements $\mathbf{U}_{\boldsymbol{\alpha},\boldsymbol{\beta}}$ are given by

$$(10) \qquad \mathbf{U}_{\boldsymbol{\alpha},\boldsymbol{\beta}} = \begin{cases} \dfrac{\boldsymbol{\beta}!}{(\boldsymbol{\beta} - \boldsymbol{\alpha} + 1)! \, 2^{|\boldsymbol{\beta} - \boldsymbol{\alpha}|}} & \text{if } \boldsymbol{\beta} - \boldsymbol{\alpha} \text{ is even}, \boldsymbol{\beta} \geq \boldsymbol{\alpha}, \\ 0 & \text{otherwise.} \end{cases}$$

We observe that $\mathbf{U}_{\boldsymbol{\alpha},\boldsymbol{\alpha}} = \boldsymbol{\alpha}! \neq 0$, so $\mathbf{U}$ is invertible and $\mathbf{D}\,\mathbf{a} = \mathbf{U}^{-1}\,\mathbf{w}$. Then,

$$\boldsymbol{\Delta}\mathbf{x}^1 \int_{\Omega_0} (q(\mathbf{x}))^2 \mathrm{d}\mathbf{x} = \boldsymbol{\Delta}\mathbf{x}^1 \sum_{|\boldsymbol{\alpha}| \leq M} \sum_{|\boldsymbol{\beta}| \leq M} a_{\boldsymbol{\alpha}} a_{\boldsymbol{\beta}} \int_{\Omega_0} \mathbf{x}^{\boldsymbol{\alpha}+\boldsymbol{\beta}} \mathrm{d}\mathbf{x}$$

$$= \sum_{|\boldsymbol{\alpha}| \leq M} \sum_{\substack{|\boldsymbol{\beta}| \leq M, \\ \boldsymbol{\alpha}+\boldsymbol{\beta} \text{ even}}} \frac{1}{2^{|\boldsymbol{\alpha}+\boldsymbol{\beta}|} \Pi(\boldsymbol{\alpha}+\boldsymbol{\beta}+1)} a_{\boldsymbol{\alpha}} a_{\boldsymbol{\beta}} \boldsymbol{\Delta}\mathbf{x}^{\boldsymbol{\alpha}+\boldsymbol{\beta}+\underline{2}}$$

$$= \sum_{|\boldsymbol{\alpha}| \leq M} a_{\boldsymbol{\alpha}} \boldsymbol{\Delta}\mathbf{x}^{\boldsymbol{\alpha}+1} \sum_{\substack{|\boldsymbol{\beta}| \leq M, \\ \boldsymbol{\alpha}+\boldsymbol{\beta} \text{ even}}} \frac{1}{2^{|\boldsymbol{\alpha}+\boldsymbol{\beta}|} \Pi(\boldsymbol{\alpha}+\boldsymbol{\beta}+1)} a_{\boldsymbol{\beta}} \boldsymbol{\Delta}\mathbf{x}^{\boldsymbol{\beta}+1}$$

$$= \langle \mathbf{D}\,\mathbf{a}, \mathbf{B}\,\mathbf{D}\,\mathbf{a} \rangle = \langle \mathbf{w}(q), \mathbf{A}\,\mathbf{w}(q) \rangle,$$

where $\mathbf{B}$ is a symmetric constant matrix whose entries are

$$(11) \qquad \mathbf{B}_{\boldsymbol{\alpha},\boldsymbol{\beta}} = \begin{cases} \dfrac{1}{\Pi(\boldsymbol{\alpha}+\boldsymbol{\beta}+1) \, 2^{|\boldsymbol{\alpha}+\boldsymbol{\beta}|}} & \text{if } \boldsymbol{\beta} + \boldsymbol{\alpha} \text{ is even}, \\ 0 & \text{otherwise,} \end{cases}$$

and $\mathbf{A} = (\mathbf{U}^{-1})^T \mathbf{B}\,\mathbf{U}^{-1}$. $\qquad\square$

Note that $\mathbf{A}$ can be viewed as an $(M+1) \times (M+1)$ block matrix by grouping its entries according to $|\boldsymbol{\alpha}|$. This generalizes the 1D case, where all blocks are 1×1.

PROPOSITION 13. *The smoothness indicator $I[q]$ of Definition 11 is a bilinear form*

$$I[q] = \langle \mathbf{v}, \mathbf{C}\,\mathbf{v} \rangle,$$

where $\mathbf{C}$ is a constant, symmetric, and positive semidefinite matrix, and $\mathbf{v}(q) = \mathbf{w}(q)/\boldsymbol{\Delta}\mathbf{x}^1$, with $\mathbf{w}(q)$ defined by (9).

Proof. From Proposition 12, we have that

$$(12) \qquad \mathbf{\Delta x^1} \int_{\Omega_0} (\partial_{\boldsymbol{\beta}} q(\mathbf{x}))^2 \mathrm{d}\mathbf{x} = \langle \mathbf{w}(\partial_{\boldsymbol{\beta}} q), \mathbf{A}\, \mathbf{w}(\partial_{\boldsymbol{\beta}} q) \rangle.$$

It is convenient to rewrite the above equation as

$$\mathbf{\Delta x}^{2\boldsymbol{\beta}+1} \int_{\Omega_0} (\partial_{\boldsymbol{\beta}} q(\mathbf{x}))^2 \mathrm{d}\mathbf{x} = \langle \mathbf{Q}^{\boldsymbol{\beta}} \mathbf{w}(q), \mathbf{A}\, \mathbf{Q}^{\boldsymbol{\beta}}\, \mathbf{w}(q) \rangle,$$

where the matrix $\mathbf{Q}^{\boldsymbol{\beta}}$ represents the shift operator $\mathbf{Q}^{\boldsymbol{\beta}} \mathbf{w}(q) = \mathbf{\Delta x}^{\boldsymbol{\beta}} \mathbf{w}(\partial_{\boldsymbol{\beta}} q)$. In fact the $\boldsymbol{\alpha}$ component of $\mathbf{Q}^{\boldsymbol{\beta}} \mathbf{w}(q)$ is given by

$$\mathbf{\Delta x}^{\boldsymbol{\beta}} (\mathbf{w}(\partial_{\boldsymbol{\beta}} q))_{\boldsymbol{\alpha}} = \mathbf{\Delta x}^{\boldsymbol{\alpha}+\boldsymbol{\beta}} \int_{\Omega_0} \partial_{\boldsymbol{\alpha}} (\partial_{\boldsymbol{\beta}}\, q(\mathbf{x}))\, \mathrm{d}\mathbf{x}$$

$$= \mathbf{\Delta x}^{\boldsymbol{\alpha}+\boldsymbol{\beta}} \int_{\Omega_0} \partial_{\boldsymbol{\alpha}+\boldsymbol{\beta}}\, q(\mathbf{x})\, \mathrm{d}\mathbf{x} = (\mathbf{w}(q))_{\boldsymbol{\alpha}+\boldsymbol{\beta}},$$

and then the entries of $\mathbf{Q}^{\boldsymbol{\beta}}$ are

$$(13) \qquad \mathbf{Q}^{\boldsymbol{\beta}}_{\boldsymbol{\alpha},\boldsymbol{\gamma}} = \begin{cases} 1 & \text{if } \boldsymbol{\gamma} = \boldsymbol{\alpha} + \boldsymbol{\beta}, \\ 0 & \text{otherwise.} \end{cases}$$

Upon introducing the vector $\mathbf{v} = \frac{\mathbf{w}}{\mathbf{\Delta x^1}}$, we have

$$I[q] = \sum_{|\boldsymbol{\beta}|=1}^{M} \mathbf{\Delta x}^{2\boldsymbol{\beta}-1} \int_{\Omega_0} (\partial_{\boldsymbol{\beta}} q(\mathbf{x}))^2 \mathrm{d}\mathbf{x} = \sum_{|\boldsymbol{\beta}|=1}^{M} \mathbf{\Delta x}^{-2} \langle \mathbf{Q}^{\boldsymbol{\beta}} \mathbf{w}, \mathbf{A}\, \mathbf{Q}^{\boldsymbol{\beta}} \mathbf{x} \rangle$$

$$= \sum_{|\boldsymbol{\beta}|=1}^{M} \langle \mathbf{Q}^{\boldsymbol{\beta}} \mathbf{v}, \mathbf{A}\, \mathbf{Q}^{\boldsymbol{\beta}} \mathbf{v} \rangle = \langle \mathbf{v}, \mathbf{C}\, \mathbf{v} \rangle,$$

where $\mathbf{C} = \sum_{|\boldsymbol{\beta}|=1}^{G} (\mathbf{Q}^{\boldsymbol{\beta}})^T\, \mathbf{A}\, \mathbf{Q}^{\boldsymbol{\beta}}$ is the smoothness measuring matrix, which is constant and symmetric. Moreover, $\mathbf{C}$ is positive semidefinite since, by (8), $I[q] \geq 0$. $\qquad \square$

For some concrete examples of the matrices $\mathbf{A}, \mathbf{Q}^{\boldsymbol{\beta}}$, and $\mathbf{C}$, see section SM1. For an alternative and more sparse representation of matrix C in one space dimension, see [3], where a suitable orthogonal basis for the polynomials is introduced.

PROPOSITION 14. *Let $\mathcal{S}$ be a stencil including Ω_0, and let $q(\mathbf{x})$ be a polynomial with $\deg q(\mathbf{x}) \geq M$ for which the components of the vector $\mathbf{v}(q)$ defined in Proposition 13 satisfy the condition*

$$(14) \qquad (\mathbf{v}(q))_{\boldsymbol{\alpha}} = \mathbf{\Delta x}^{\boldsymbol{\alpha}-1} \int_{\Omega_j} \partial_{\boldsymbol{\alpha}} q(\mathbf{x}) \mathrm{d}\mathbf{x} = \sum_{\substack{|\boldsymbol{\beta}|=0, \\ \boldsymbol{\beta}\ even}}^{M-|\boldsymbol{\alpha}|} \frac{\partial_{\boldsymbol{\alpha}+\boldsymbol{\beta}} u(\mathbf{0})}{2^{|\boldsymbol{\beta}|}(\boldsymbol{\beta}+1)!} \mathbf{\Delta x}^{\boldsymbol{\beta}+\boldsymbol{\alpha}} + \mathcal{O}(\rho^{M+1}),$$

for a regular function $u(\mathbf{x})$ and $1 \leq |\boldsymbol{\alpha}| \leq M$; then

$$I[q] = B_M + R[q],$$

where B_M depends on M but not on $q(\mathbf{x})$.

Proof. We define $\mathbf{v}(q) = \mathbf{v}^{B_M} + \mathbf{v}^{R[q]}$ with

$$(\mathbf{v}^{B_M})_{\boldsymbol{\alpha}} := \begin{cases} \displaystyle\sum_{\substack{|\boldsymbol{\beta}|=0, \\ \boldsymbol{\beta} \text{ even}}}^{M-|\boldsymbol{\alpha}|} \frac{\partial_{\boldsymbol{\alpha}+\boldsymbol{\beta}} u(\mathbf{0})}{2^{|\boldsymbol{\beta}|}(\boldsymbol{\beta}+\mathbf{1})!} \boldsymbol{\Delta}\mathbf{x}^{\boldsymbol{\beta}+\boldsymbol{\alpha}}, & 1 \leq |\boldsymbol{\alpha}| \leq M, \\[2em] 0, & |\boldsymbol{\alpha}| = 0 \text{ and } |\boldsymbol{\alpha}| > M, \end{cases}$$

and observe that

$$(\mathbf{v}^{R[q]})_{\boldsymbol{\alpha}} = \mathcal{O}(\rho^{M+1}).$$

As in Corollary 3 in [16], using Proposition 13, the thesis holds with

$$B_M := \langle \mathbf{v}^{B_M}, \mathbf{C}\,\mathbf{v}^{B_M} \rangle, \qquad R[q] := 2\langle \mathbf{v}^{B_M}, \mathbf{C}\,\mathbf{v}^{R[q]} \rangle + \langle \mathbf{v}^{R[q]}, \mathbf{C}\,\mathbf{v}^{R[q]} \rangle. \qquad \square$$

The actual size of B_M and of the remainder $R[q]$ depends on the presence of a critical point in the data.

DEFINITION 15. *A smooth enough function is said to have a* critical point of order n_{cp} *in* $\hat{\mathbf{x}}$ *if* $\partial_{\boldsymbol{\alpha}} u(\hat{\mathbf{x}}) = 0$ *for every* $|\boldsymbol{\alpha}| \leq n_{cp}$ *and if* $\partial_{\boldsymbol{\alpha}} u(\mathbf{0}) \neq 0$ *for at least one multi-index with* $|\boldsymbol{\alpha}| = n_{cp} + 1$. *If* $n_{cp} = 0$, *the function will be called* regular.

COROLLARY 16. *Assume that the hypotheses of Proposition 14 hold. If there is a critical point with* $n_{cp} \geq M$, *we have* $B_M = 0$ *and* $R[q] = \mathcal{O}(\rho^{2M+2})$. *In the case* $n_{cp} < M$, *we have* $B_M = \mathcal{O}(\rho^{2(n_{cp}+1)})$ *and* $R[q] = \mathcal{O}(\rho^{M+2+n_{cp}})$, *so that* $R[q] = o(B_M)$.

Proof. Only the derivatives of orders $|\boldsymbol{\alpha}| \leq M$ appear in $(\mathbf{v}^{B_M})_{\boldsymbol{\alpha}}$. If $n_{cp} \geq M$, they all vanish and we have $\mathbf{v}^{B_M} = \mathbf{0}$ and $B_M = 0$. Then $R[q]$ depends only on $\mathbf{v}^{R[q]}$, so $R[q] = \mathcal{O}(\rho^{2M+2})$. Otherwise, $n_{cp} < M$ and $\min_{1 \leq |\boldsymbol{\alpha}| \leq M} \theta((\mathbf{v}^{B_M})_{\boldsymbol{\alpha}}) = n_{cp} + 1$. Then $\theta(B_M) = 2n_{cp} + 2$ and $\theta(R[q]) = M + n_{cp} + 2$, so $\theta(R[q]) > \theta(B_M)$, i.e., $R[q] = o(B_M)$. $\square$

Remark 17. In view of Remark 6, we point out that if $P_1(\mathbf{x}), P_2(\mathbf{x}), \ldots, P_m(\mathbf{x})$ and $P_{\mathsf{opt}}(\mathbf{x})$ satisfy Proposition 14 with the same $u(\mathbf{x})$, then $P_0(\mathbf{x})$ satisfies the same proposition since $\mathbf{w}(q)$, and then $\mathbf{v}(q)$, are linear in q.

Example 18. In the one-dimensional CWENO and CWENOZ reconstructions of order 3, we have that the polynomials $P_1(x), P_2(x) \in \mathbb{P}_1^1$ and $P_{\mathsf{opt}}(x), P_0(x) \in \mathbb{P}_1^2$ satisfy the hypothesis of Proposition 14 with $M = 1$. We have $B_1 = u'(0)^2 \Delta x^2$ and

$$\begin{aligned} I[P_1] &= B_1 - u'(0)u''(0)\Delta x^3 + \mathcal{O}(\Delta x^4), \\ I[P_2] &= B_1 + u'(0)u''(0)\Delta x^3 + \mathcal{O}(\Delta x^4), \\ I[P_{\mathsf{opt}}] &= B_1 + \mathcal{O}(\Delta x^4), \\ I[P_0] &= B_1 + \frac{d_1 - d_2}{d_0} u'(0)u''(0)\Delta x^3 + \mathcal{O}(\Delta x^4), \end{aligned}$$

and thus $R[P_1], R[P_2], R[P_0]$ are $\mathcal{O}(\Delta x^3)$, while $R[P_{\mathsf{opt}}]$ is $\mathcal{O}(\Delta x^4)$. (See also [15].)

Example 19. In the one-dimensional CWENO and CWENOZ reconstructions of order 5, we have that $P_1(x), P_2(x), P_3(x) \in \mathbb{P}_1^2$ and $P_{\mathsf{opt}}(x) \in \mathbb{P}_1^4$ satisfy the hypothesis of Proposition 14 with $M = 2$. We have $B_2 = u'(0)^2 \Delta x^2 + \frac{13}{12} u''(0)^2 \Delta x^4$, and $R[P_{\mathsf{opt}}]$, $R[P_1]$, $R[P_2]$, $R[P_3]$ are all $\mathcal{O}(\Delta x^4)$. The Taylor expansions are reported in section SM2.1.

Example 20. In the one-dimensional CWENOZ reconstructions of order 7, we have that $P_1(x), P_2(x), P_3(x), P_4(x) \in \mathbb{P}_1^3$ and $P_{\mathsf{opt}}(x) \in \mathbb{P}_1^6$ satisfy the hypothesis of Proposition 14 with $M = 3$, $B_3 = u'(0)^2 \Delta x^2 + (\frac{13}{12} u''(0)^2 + \frac{1}{12} u'(0) u'''(0)) \Delta x^4 + \frac{1043}{960} u'''(0)^2 \Delta x^6$, and $R[P_1], \ldots, R[P_4]$ are $\mathcal{O}(\Delta x^5)$, while $R[P_{\mathsf{opt}}]$ is $\mathcal{O}(\Delta x^6)$. For the details of the Taylor expansions, see section SM2.2.

In the following, we will consider $q(\mathbf{x}) \in \{P_1(\mathbf{x}), \ldots, P_m(\mathbf{x}), P_{\mathsf{opt}}(\mathbf{x})\}$, so to simplify notation we write $R_k = R[P_k]$ for $k = 1, \ldots, m$ and $R_0 = R[P_{\mathsf{opt}}]$.

In order to obtain a computationally cheap CWENOZ reconstruction procedure, we follow the idea of [5] and of the later WENOZ [11, 16] constructions and define the global smoothness indicator τ as a linear combination of the other smoothness indicators $I_0, \ldots, I_m$.

DEFINITION 21. *The global regularity indicator of a* CWENOZ *scheme is defined as a linear combination*

$$(15) \qquad \tau := \left| \sum_{k=0}^{m} \lambda_k I_k \right|$$

for some choice of coefficients $\lambda_0, \ldots, \lambda_m$ *such that* $\sum_{k=0}^{m} \lambda_k = 0$.

We point out that the idea to include the smoothness indicator of P_{opt} in (15) was also exploited, in the WENO context, by [42] to define an improved WENOZ.

In the next section we will study the optimal choice for the coefficients λ_k in (15), but first we prove some general results using only the assumption of Definition 21.

COROLLARY 22. *Proposition* 14 *implies that* $\tau = |B_M \sum_{k=0}^{m} \lambda_k + \sum_{k=0}^{m} \lambda_k R_k|$, *so, thanks to the hypothesis* $\sum_k \lambda_k = 0$, $\tau = \mathcal{O}(\sum_{k=0}^{m} R_k)$.

We point out that this result is independent of the grid, and relies only on the approximation accuracy of the polynomials included in the CWENOZ construction.

2.3. Order of accuracy of a CWENOZ scheme. A CWENOZ reconstruction is a combination of polynomials, each of which is accurate of order $g + 1$, and we are interested in designing the nonlinear weights of the combination such that, for smooth data, the accuracy of the reconstruction polynomial $P_{\mathsf{rec}}^{\mathsf{CWZ}}$ is boosted to the accuracy of P_{opt}, i.e., to $G + 1$. In this section we exploit the sufficient condition of Remark 5 in order to choose the optimal values for the parameters ℓ and ϵ appearing in (6b).

Let us first point out that, although ϵ cannot be taken exactly 0, a small value of ϵ will reduce the spurious oscillations close to discontinuities. As in [2, 16, 28, 15], we allow a dependence of ϵ on the cell size, namely $\epsilon = \rho^{\hat{m}}$, with an exponent $\hat{m}$ that we would like to choose as large as possible without affecting the accuracy on smooth flows. Regarding the parameter ℓ, it should be taken as small as possible: high values for ℓ enhance the ratios between the indicators of the polynomials and make the reconstruction more dissipative on discontinuous solutions, as pointed out in [16]. The main result of this section is that a proper choice for the global smoothness indicator τ will help to obtain optimal reconstruction order with small ℓ and ϵ.

We will make use of the following result, which was proved in [16].

LEMMA 23 (Lemma 6 of [16]). *If for* $k = 0, \ldots, m$, $\gamma > 0$, *and* A *independent on* k, *we have* $\alpha_k^Z = d_k \left(1 + A\rho^\gamma + \mathcal{O}\left(\rho^{\gamma+1}\right) \right)$, *then* $\omega_k^{CWZ} - d_k = \mathcal{O}(\rho^{\gamma+1})$ *for* $k = 0, \ldots, m$.

The accuracy of a CWENOZ reconstruction is expressed by the following result.

THEOREM 24. *Assume that the polynomials $P_1(\mathbf{x}), \dots, P_m(\mathbf{x})$ and $P_{\mathsf{opt}}(\mathbf{x})$ in a* CWENOZ *reconstruction satisfy Proposition* 14 *for some M and the same $u(x)$ and that the parameters $\epsilon = C_\epsilon \rho^{\hat{m}}$, for some $C_\epsilon \neq 0$, and ℓ in* (6b) *satisfy*

$$\text{(16a)} \qquad\qquad \hat{m} \leq 2M + 1,$$

$$\text{(16b)} \qquad\qquad \ell(2M + 2 - \hat{m}) \geq G - g - 1,$$

$$\text{(16c)} \qquad\qquad \ell\left[\theta(\tau)|_{n_{cp}=0} - \min(\hat{m}, 2M)\right] \geq G - g - 1.$$

Then, on smooth data, the CWENOZ *reconstruction achieves the optimal order of accuracy $G + 1$ as $\rho \to 0$.*

As seen in Remark 5, it is sufficient to verify that $\theta(\omega_k^Z - d_k) \geq G - g$. We consider separately the cases $n_{cp} \geq M$ and $n_{cp} < M$.

Proof for $n_{cp} \geq M$. Corollary 16 ensures that $B_M = 0$ and $\theta(R_k) \geq 2M + 2$, and, together with Corollary 22, we have that

$$I_k = C_k \rho^{2M+2} + \mathcal{O}(\rho^{2M+3}) \quad \text{and} \quad \tau = C_\tau \rho^{2M+2} + \mathcal{O}(\rho^{2M+3})$$

for some, possibly null, constants $C_0, \dots, C_m, C_\tau$ that do not depend on ρ. Then $\alpha_k^Z = d_k\left(1 + \gamma_k^\ell\right)$ for

$$\gamma_k = \frac{\tau}{I_k + \epsilon} = \frac{C_\tau \rho^{2M+2} + \mathcal{O}(\rho^{2M+3})}{C_k \rho^{2M+2} + \mathcal{O}(\rho^{2M+3}) + C_\epsilon \rho^{\hat{m}}}.$$

For convergence it is of course necessary that $\gamma_k \to 0$ and thus that $\hat{m} \leq 2M + 1$, as in (16a). Under this hypothesis,

$$\gamma_k \sim \frac{C_\tau}{C_\epsilon} \rho^{2M+2-\hat{m}} = C\rho^{2M+2-\hat{m}}$$

for some, possibly null, constant C that does not depend on ρ. Thus,

$$\alpha_k^Z \sim d_k\left(1 + C^\ell \rho^{\ell(2M+2-\hat{m})}\right),$$

and $\ell(2M + 2 - \hat{m}) \geq \ell \geq 1$. This allows us to apply Lemma 23 and to conclude that

$$\text{(17)} \qquad\qquad \theta(\omega_k^Z - d_k) \geq \ell(2M + 2 - \hat{m}) + 1 \geq G - g$$

for $n_{cp} \geq M$, which concludes the proof for this case thanks to (16b). $\qquad\square$

Proof for $n_{cp} < M$. In this case,

$$\gamma_k = \frac{\tau}{I_k + \epsilon} = \frac{\tau}{B_M + \epsilon} \frac{1}{1 + \frac{R_k}{B_M + \epsilon}} = \frac{\tau}{B_M + \epsilon}(1 + o(1)),$$

provided that $b_k = \frac{R_k}{B_M + \epsilon} \to 0$. However, this is true for any $\hat{m} \geq 0$ since Corollary 16 states that $B_M \neq 0$ and $R_k / B_M \to 0$. Then $\gamma_k \sim C\rho^t$ for a constant $C \neq 0$, and

$$t = \theta(\tau) - \theta(B_M + \epsilon) = \theta(\tau) - \min\left(\theta(B_M), \hat{m}\right).$$

Corollary 16 implies that $\theta(B_M) = 2n_{cp} + 2$ and, together with Corollary 22, that $\theta(\tau) \geq \theta(R_k) = M + n_{cp} + 2$, so that $t \geq M - n_{cp} \geq 1$.

Finally, we have $\alpha_k^Z = d_k \left(1 + \gamma_k^\ell\right) \sim d_k \left(1 + C^\ell \rho^{\ell t}\right)$ with $\ell t \geq 1$, and thus Lemma 23, together with $\theta(B_M) = 2n_{cp} + 2$, implies that

$$(18) \qquad \theta(\omega_k^Z - d_k) \geq 1 + \ell t = 1 + \ell\big[\theta(\tau) - \min\left(2n_{cp} + 2, \hat{m}\right)\big].$$

Since the minimum value of $\theta(\tau)$ is attained when $n_{cp} = 0$, we have that

$$\theta(\omega_k^Z - d_k) \geq 1 + \ell\big[\theta(\tau)|_{n_{cp}=0} - \min(\hat{m}, 2M)\big] \geq G - g,$$

which concludes the proof for this case too thanks to (16c). □

Note that bounds for $\theta(\omega_k - d_k)$ for each specific choice of $\hat{m}, \ell$ and in the presence of a critical point of order n_{cp} are given by (17) if $n_{cp} \geq M$ and by (18) otherwise.

Remark 25. Since P_0 satisfies Proposition 14 (see Remark 17), Theorem 24 is also true for $I_0 = I[P_0]$ in Definition 3.

Remark 26. We point out that condition (16b) is always satisfied if ℓ is taken large enough. If $\theta(\tau) \geq 2M + 1$, the same is true for (16c), and thus for all $\hat{m} \leq 2M+1, \exists\, \ell \geq 1$ such that the CWENOZ is convergent with optimal order. On the other hand if $\theta(\tau) \leq 2M$, (16c) can be satisfied only when $\hat{m} < \theta(\tau)$. In this case, $\exists\, \ell \geq 1$ such that the CWENOZ is convergent with optimal order only for $\hat{m} < \theta(\tau) < 2M+1$. Moreover, we point out that (16) implies that a larger value of $\theta(\tau)$ allows us to use a smaller ϵ and a smaller power parameter ℓ. This allows us to design CWENOZ schemes that outperform their CWENO counterparts.

3. Optimal CWENOZ reconstructions.

3.1. CWENOZ in one space dimension. In the CWENOZ reconstruction of order $2r - 1$, we employ the stencils and polynomials defined in Example 7, as in [13]. In that paper, however, we considered the same global smoothness indicators τ_{2r-1} that are optimal for WENOZ (see [16]), which are based on the r polynomials of degree $r - 1$, i.e., $\lambda_0 = 0$ in (15). Now we allow $\lambda_0 \neq 0$, and we will denote by $\hat{\tau}_{2r-1}$ the optimal definition of the global smoothness indicator for CWENOZ of order $2r - 1$. The following lemma is a generalization of Examples 18, 19, and 20 for an arbitrary polynomial.

LEMMA 27. *Let $q(x)$ be a polynomial of degree at least γ, interpolating a set of consecutive cell averages of $u(x)$ in the sense of (4), with stencils as in Example 7. Then $q(x)$ satisfies the hypothesis of Proposition 14 for any $M \leq \gamma$.*

Proof. We note that $q(x)$ is the derivative of the polynomial $Q(x)$ that interpolates the regular function $U(x) = \int_{-\infty}^x u(t)\, dt$ in the $\gamma+2$ points delimiting $\gamma+1$ consecutive cells. Then $|U(x) - Q(x)| = \mathcal{O}(\Delta x^{\gamma+2})$, and we have, for any $0 \leq \alpha \leq \gamma$,

$$\begin{aligned}
(\mathbf{v}(q))_\alpha &= \Delta x^{\alpha-1} \int_{-\frac{\Delta x}{2}}^{\frac{\Delta x}{2}} \partial_\alpha\, q(x) dx = \Delta x^{\alpha-1} \int_{-\frac{\Delta x}{2}}^{\frac{\Delta x}{2}} \partial_{\alpha+1}\, Q(x)\, dx \\
&= \Delta x^{\alpha-1} \int_{-\frac{\Delta x}{2}}^{\frac{\Delta x}{2}} \left(\partial_{\alpha+1} U(x) + \mathcal{O}(\Delta x^{\gamma+2-\alpha-1})\right)\, dx \\
&= \Delta x^{\alpha-1} \int_{-\frac{\Delta x}{2}}^{\frac{\Delta x}{2}} \partial_\alpha u(x)\, dx + \mathcal{O}(\Delta x^{\gamma+1}) \\
&= \sum_{\substack{\beta=0, \\ \beta \text{ even}}}^{\gamma-\alpha} \frac{\partial_{\alpha+\beta} u(0)}{2^\beta (\beta+1)!} \Delta x^{\beta+\alpha} + \mathcal{O}(\Delta x^{\gamma+1}).
\end{aligned}$$

□

From Corollary 22, we know that $\tau = |\sum_{k=0}^{r} \lambda_k I_k| = \mathcal{O}(\sum_{k=0}^{m} R_k)$ whenever $\sum \lambda_k = 0$, and any choice of coefficients λ_k sum up to 0 would define a τ for CWENOZ that generalizes the nonoptimal definition of τ in [11]. However, by closely examining each case, it is possible to obtain an even smaller τ, as is the case for the optimal definition for WENOZ given in [16].

CWENOZ3. In CWENOZ3 (see [15]) we have

$$I_1 = I[P_1] = B_1 - u'(0)u''(0)\Delta x^3 + \left(\frac{5}{12}u'(0)u'''(0) + \frac{1}{4}u''(0)^2 \right)\Delta x^4 + \mathcal{O}(\Delta x^5),$$

$$I_2 = I[P_2] = B_1 + u'(0)u''(0)\Delta x^3 + \left(\frac{5}{12}u'(0)u'''(0) + \frac{1}{4}u''(0)^2 \right)\Delta x^4 + \mathcal{O}(\Delta x^5),$$

$$I_0 = I[P_{\mathsf{opt}}] = B_1 + \left(\frac{5}{12}u'(0)u'''(0) + \frac{13}{12}u''(0)^2 \right)\Delta x^4 + \mathcal{O}(\Delta x^5).$$

Thus any set of coefficients such that $\lambda_1 = \lambda_2$ and $\lambda_0 = -2\lambda_1$ cancels all terms up to $\mathcal{O}(\Delta x^3)$, but it is never possible to cancel all the $\mathcal{O}(\Delta x^4)$ terms. So we define

$$(19) \qquad\qquad \hat{\tau}_3 = |tI_1 + tI_2 - 2tI_0|,$$

and, for any $t \in \mathbb{R}$, we have that $\theta(\hat{\tau}_3) = 4$. $\hat{\tau}_3$ allows us to employ a smaller ϵ than τ_3 of [13], since $\theta(\tau_3) = 3$.

Remark 28. We have explored also the possibility of defining $I_0 = I[P_0]$, as in previous works on CWENO (Remark 6). Convergence is established by Remark 25. In this case, assuming symmetry of the linear coefficients, we have $d_0 = (1 - d_1 - d_2) = 1 - 2d_1$, and the indicator I_0 depends on d_0 as

$$I_0 = I[P_0] = B_1 + \left(\frac{5}{12}u'(0)u'''(0) + \frac{13}{12d_0^2}u''(0)^2 \right)\Delta x^4 + \mathcal{O}(\Delta x^5).$$

However, it is easy to verify that no values of λ_k or d_0 can improve $\hat{\tau}_3$ to $\theta(\hat{\tau}_3) = 5$.

For CWENOZ3, $\theta(\hat{\tau}_3) \geq 3 = 2M + 1$, and thus we obtain the optimal order of convergence for all $\hat{m} \leq 3$, and in particular conditions (16) are satisfied for all $\ell \geq 1$.

We have conducted a thorough study to check the conditions given by Theorem 24. We report in Table 1, as an example, only the most difficult case, i.e., the case of a critical point with $n_{cp} = 1$. A grid of size Δx was set up with a cell center in the critical point of the function $\sin(\pi x - \sin(\pi x)/\pi)$ located at about $x_{\mathrm{crit}} \simeq 0.596683186911209$; see [24]. The cell averages of this cell and of its immediate neighbors were initialized with the 2-point Gaussian quadrature rule. Next, the CWENOZ3 reconstruction was computed for the cell containing the critical point. Due to the very fine grids employed, all computations were performed in quadruple precision.

In Table 1 we show the case of $\ell = 2$ and compare three values for $\hat{m}$. First, τ decays proportionally to Δx^4, as indicated above. When $\hat{m} = 2$, the rate of decay of the distance between the nonlinear weights and the optimal ones is 6, and the reconstruction error is already of order 3 on very coarse grids. When $\hat{m} = 3$, the rate of decay of the nonlinear weights approaches 3 very slowly, and the reconstruction error is of order 3 only on very fine grids. When $\hat{m} = 4$, the nonlinear weights do not tend to the linear ones, and the reconstruction error is of order 2. All findings are in agreement with the results of Theorem 24.

TABLE 1

τ, $\max_{k=0,1,2}\{|\omega_k^Z - d_k|\}$, and reconstruction errors for the CWENOZ3 reconstruction on a critical point with $n_{cp} = 1$.

			$\ell = 2, \hat{m} = 2$				$\ell = 2, \hat{m} = 3$				$\ell = 2, \hat{m} = 4$			
Δx	τ	rate	$\omega^Z - d$	rate	error	rate	$\omega^Z - d$	rate	error	rate	$\omega^Z - d$	rate	error	rate
5.0e-02	1.4e-03	—	1.7e-02	—	2.5e-04	—	4.4e-01	—	1.8e-03	—	5.6e-01	—	2.8e-03	—
2.5e-02	9.1e-05	3.99	4.8e-04	5.11	3.9e-05	2.66	3.4e-01	0.38	2.9e-04	2.63	5.6e-01	0.01	5.8e-04	2.26
1.3e-02	5.7e-06	4.00	8.7e-06	5.79	5.0e-06	2.97	2.1e-01	0.70	4.1e-05	2.83	5.6e-01	0.00	1.3e-04	2.15
6.3e-03	3.6e-07	4.00	1.4e-07	5.95	6.3e-07	2.99	9.2e-02	1.18	4.2e-06	3.27	5.6e-01	0.00	3.1e-05	2.08
3.1e-03	2.2e-08	4.00	2.2e-09	5.99	7.9e-08	3.00	2.7e-02	1.76	2.8e-07	3.94	5.6e-01	0.00	7.4e-06	2.04
1.6e-03	1.4e-09	4.00	3.5e-11	6.00	9.8e-09	3.00	5.6e-03	2.28	8.2e-09	5.06	5.6e-01	0.00	1.8e-06	2.02
7.8e-04	8.7e-11	4.00	5.4e-13	6.00	1.2e-09	3.00	9.0e-04	2.64	5.1e-10	4.03	5.6e-01	0.00	4.5e-07	2.01
3.9e-04	5.4e-12	4.00	8.5e-15	6.00	1.5e-10	3.00	1.3e-04	2.83	1.3e-10	1.98	5.6e-01	0.00	1.1e-07	2.01
1.9e-04	3.4e-13	4.00	1.3e-16	6.00	1.9e-11	3.00	1.7e-05	2.92	1.8e-11	2.80	5.6e-01	0.00	2.8e-08	2.00
9.8e-05	2.1e-14	4.00	2.1e-18	6.00	2.4e-12	3.00	2.2e-06	2.96	2.4e-12	2.95	5.6e-01	0.00	7.1e-09	2.00
4.9e-05	1.3e-15	4.00	3.2e-20	6.00	3.0e-13	3.00	2.7e-07	2.98	3.0e-13	2.99	5.6e-01	0.00	1.8e-09	2.00
2.4e-05	8.3e-17	4.00	5.1e-22	6.00	3.7e-14	3.00	3.4e-08	2.99	3.7e-14	3.00	5.6e-01	-0.00	4.4e-10	2.00
1.2e-05	5.2e-18	4.00	7.9e-24	6.00	4.7e-15	3.00	4.3e-09	3.00	4.7e-15	3.00	5.6e-01	-0.00	1.1e-10	2.00
6.1e-06	3.2e-19	4.00	1.2e-25	6.00	5.9e-16	3.00	5.4e-10	3.00	5.9e-16	3.00	5.6e-01	-0.00	2.7e-11	2.00

TABLE 2

Upper bound for the sensitivity order $\hat{m}$ in 1D CWENOZ reconstructions of Example 7.

r	2r-1	$\theta(\hat{\tau}_{2r-1})$	$\ell = 1$	$\ell = 2$	$\ell = 3$	$\ell = 4$	$\ell = 5$	$\ell = 6$
2	3	4	3	3	3	3	3	3
3	5	6	5	5	5	5	5	5
4	7	7	6	7	7	7	7	7
5	9	8	5	6	7	7	7	7
6	11	9	5	7	7	8	8	8

CWENOZ5. For CWENOZ5 we have (see [14]) $I_k = B_2 + \mathcal{O}(\Delta x^4)$ with $B_2 = u'(0)^2 \Delta x^2 + \frac{13}{12} u''(0)^2 \Delta x^4$. The Taylor expansions of the indicators are reported in section SM2.1. We can thus obtain $\theta(\hat{\tau}_5) = 6$ with any choice

$$(20) \qquad \hat{\tau}_5 = |tI_1 + 4tI_2 + tI_3 - 6tI_0|, \qquad t \in \mathbb{R},$$

and no value of t can lead to an improvement. In any case, this is better than the situation for WENOZ and for the CWENOZ of [13], where one has only $\theta(\tau_5) = 5$.

Also in this case we have explored the choice $I_0 = I[P_0]$ (see Remark 25), but no value of λ_k or of the linear coefficients has led to any improvement.

For CWENOZ5, $\theta(\hat{\tau}) \geq 5 = 2M + 1$, and then we obtain the optimal order of convergence for all $\hat{m} \leq 5$, and in particular (16a)–(16c) are satisfied for all $\ell \geq 1$.

CWENOZ *of orders higher than* 5. Proceeding in a similar manner, we obtain for CWENOZ7, CWENOZ9, and CWENOZ11, respectively,

$$\hat{\tau}_7 = |-tI_1 - 3tI_2 + 3tI_3 + tI_4|, \qquad \theta(\hat{\tau}_7) = 7$$
$$\hat{\tau}_9 = |tI_1 + (2t + u)I_2 + (3u - 6t)I_3 + (2t + u)I_4 + tI_5 - 5uI_0|, \quad \theta(\hat{\tau}_9) = 8$$
$$\hat{\tau}_{11} = |(u - s)I_1 + (37u - t)I_2 + (10s + 118u - 2t)I_3$$
$$+ (2t - 10s + 54u)I_4 + tI_5 + sI_6 - 210uI_0|, \qquad \theta(\hat{\tau}_{11}) = 9,$$

where the parameters t, s, u can take any real values. More details for the first and second cases can be found in sections SM2.2 and SM2.3. In these three cases, we have obtained a $\hat{\tau}$ of the same order as the τ in [13], and the global smoothness indicators of [13] correspond to the choice $t = 1$ in $\hat{\tau}_7$, $u = 0$, $t = 1$ in $\hat{\tau}_9$, and $u = 0$, $t = 1$, $s = t$ in $\hat{\tau}_{11}$.

In the case of CWENOZ7 again, the optimal order of convergence is possible for $\hat{m} \leq 7$, but (16) requires $\ell \geq 2$ if $\hat{m} = 7$. Condition (16c) can be satisfied only for $\hat{m} \leq 7$ for CWENOZ9 and for $\hat{m} \leq 8$ in the CWENOZ11 case.

We summarize the result of this section in Table 2, where we report the possible choices for the order $\hat{m}$ of the sensitivity parameter ϵ for various choices of ℓ in (6b).

3.2. CWENOZ3 in two space dimensions. We now consider the third order reconstruction of [34], restricted to the Cartesian uniform grid case, as in [12]. The stencil for the reconstruction is the patch of 3×3 cells centered in the cell in which the reconstruction is sought. The optimal polynomial $P_{\text{opt}}^{(2)}(\mathbf{x})$ is the polynomial of degree 2, defined on $\eta = 9$ cells as in (4). Additionally, we consider $m = 4$ polynomials of degree 1 that fit four cell averages in a sector of the main stencil. In particular, we denote by $P_{NE}(\mathbf{x}) \equiv P_1^{(1)}(\mathbf{x})$ the polynomial of degree 1 that interpolates exactly the central cell average and, in a least squares sense, the three cells located in the north, east, and northeast directions; $P_{SE}(\mathbf{x}) \equiv P_2^{(1)}(\mathbf{x}), P_{SW}(\mathbf{x}) \equiv P_3^{(1)}(\mathbf{x}), P_{NW}(\mathbf{x}) \equiv P_4^{(1)}(\mathbf{x})$ denote the analogous polynomials in the southeast, southwest, and northwest substencils, respectively. The expression for all of the polynomials involved is given in [12] and is reported here for convenience.

As in [34], we employ a polynomial basis such that all nonconstant basis elements have zero mean in the central cell. Considering $\boldsymbol{\Delta}\mathbf{x} = (h, k)$, we have,

$$\begin{aligned} \varphi_{(0,0)}(\mathbf{x}) &= 1, & \varphi_{(1,0)}(\mathbf{x}) &= x, & \varphi_{(0,1)}(\mathbf{x}) &= y, \\ \varphi_{(2,0)}(\mathbf{x}) &= x^2 - \tfrac{h^2}{12}, & \varphi_{(0,2)}(\mathbf{x}) &= y^2 - \tfrac{k^2}{12}, & \varphi_{(1,1)}(\mathbf{x}) &= xy. \end{aligned}$$

In this basis, we have

$$P_{\text{opt}}^{(2)}(\mathbf{x}) = \overline{u}_0 + \sum_{|\boldsymbol{\beta}|=1}^{2} c_{\boldsymbol{\beta}}^{(2)} \varphi_{\boldsymbol{\beta}}(\mathbf{x}) \text{ and } P_j^{(1)}(\mathbf{x}) = \overline{u}_0 + \sum_{|\boldsymbol{\beta}|=1} c_{\boldsymbol{\beta}}^j \varphi_{\boldsymbol{\beta}}(\mathbf{x}), \ j = 1, \dots, 4,$$

with coefficients computed in [12].

This example satisfies the hypothesis of Proposition 14 with $1 \leq |\boldsymbol{\alpha}| \leq M = 1$. In fact, when we substitute the Taylor expansions of the cell averages (equation (SM5) in section SM2.4) into the coefficients of the polynomials given in [12], for $|\boldsymbol{\alpha}| = 1$ we obtain

$$c_{\boldsymbol{\alpha}}^{(2)} = \frac{1}{\boldsymbol{\alpha}!} \partial_{\boldsymbol{\alpha}} u \Big|_0 + \mathcal{O}(\rho^2) \text{ and } c_{\boldsymbol{\alpha}}^r = \frac{1}{\boldsymbol{\alpha}!} \partial_{\boldsymbol{\alpha}} u \Big|_0 + \mathcal{O}(\rho), \qquad r = 1, \dots, 4.$$

We consider $q(\mathbf{x}) \in \{P_1^{(1)}(\mathbf{x}), \dots, P_4^{(1)}(\mathbf{x}), P_{\text{opt}}^{(2)}(\mathbf{x})\}$. The basis functions $\varphi_{\boldsymbol{\beta}}(\mathbf{x})$ differ from the monomial basis only for constant terms, and we have, for $|\boldsymbol{\alpha}| = 1$,

$$\begin{aligned} (\mathbf{v}(q))_{\boldsymbol{\alpha}} &= \boldsymbol{\Delta}\mathbf{x}^{\boldsymbol{\alpha}-1} \int_{\Omega_0} \partial_{\boldsymbol{\alpha}} q(\mathbf{x}) \mathrm{d}\mathbf{x} = \boldsymbol{\Delta}\mathbf{x}^{\boldsymbol{\alpha}-1} \sum_{|\boldsymbol{\beta}|=1}^{\gamma} c_{\boldsymbol{\beta}} \int_{\Omega_0} \partial_{\boldsymbol{\alpha}} \varphi_{\boldsymbol{\beta}}(\mathbf{x}) \mathrm{d}\mathbf{x} \\ &= \sum_{\substack{|\boldsymbol{\beta}| \leq \gamma, \boldsymbol{\beta} \geq \boldsymbol{\alpha}, \\ \boldsymbol{\beta}-\boldsymbol{\alpha} \text{ even}}} c_{\boldsymbol{\beta}} \frac{\boldsymbol{\beta}!}{(\boldsymbol{\beta}-\boldsymbol{\alpha}+1)! \, 2^{|\boldsymbol{\beta}-\boldsymbol{\alpha}|}} \boldsymbol{\Delta}\mathbf{x}^{\boldsymbol{\beta}+1} = \boldsymbol{\alpha}! \, c_{\boldsymbol{\alpha}} \boldsymbol{\Delta}\mathbf{x}^{\boldsymbol{\alpha}} \\ &= \partial_{\boldsymbol{\alpha}} u \Big|_0 \boldsymbol{\Delta}\mathbf{x}^{\boldsymbol{\alpha}} + \mathcal{O}(\rho^2), \end{aligned}$$

with $\gamma = 1$ if $c_{\boldsymbol{\beta}} = c_{\boldsymbol{\beta}}^r$, $r = 1, \dots, 4$, and $\gamma = 2$ if $c_{\boldsymbol{\beta}} = c_{\boldsymbol{\beta}}^{(2)}$.

In order to simplify the notation, we consider square cells, i.e., $h = k$. From

Proposition 13 (see also section SM1), using again the expansions (SM5), we have

$$
\begin{aligned}
I_{NE} &= B_1 + \left(u_x\big|_{\mathbf{0}}u_{xx}\big|_{\mathbf{0}} + \tfrac{2}{3}u_x\big|_{\mathbf{0}}u_{xy}\big|_{\mathbf{0}} + \tfrac{2}{3}u_y\big|_{\mathbf{0}}u_{xy}\big|_{\mathbf{0}} + u_y\big|_{\mathbf{0}}u_{yy}\big|_{\mathbf{0}}\right)h^3 + \mathcal{O}(\rho^4),\\
I_{NW} &= B_1 + \left(u_x\big|_{\mathbf{0}}u_{xx}\big|_{\mathbf{0}} + \tfrac{2}{3}u_x\big|_{\mathbf{0}}u_{xy}\big|_{\mathbf{0}} - \tfrac{2}{3}u_y\big|_{\mathbf{0}}u_{xy}\big|_{\mathbf{0}} + u_y\big|_{\mathbf{0}}u_{yy}\big|_{\mathbf{0}}\right)h^3 + \mathcal{O}(\rho^4),\\
I_{SE} &= B_1 + \left(u_x\big|_{\mathbf{0}}u_{xx}\big|_{\mathbf{0}} - \tfrac{2}{3}u_x\big|_{\mathbf{0}}u_{xy}\big|_{\mathbf{0}} + \tfrac{2}{3}u_y\big|_{\mathbf{0}}u_{xy}\big|_{\mathbf{0}} - u_y\big|_{\mathbf{0}}u_{yy}\big|_{\mathbf{0}}\right)h^3 + \mathcal{O}(\rho^4),\\
I_{SW} &= B_1 + \left(-u_x\big|_{\mathbf{0}}u_{xx}\big|_{\mathbf{0}} - \tfrac{2}{3}u_x\big|_{\mathbf{0}}u_{xy}\big|_{\mathbf{0}} - \tfrac{2}{3}u_y\big|_{\mathbf{0}}u_{xy}\big|_{\mathbf{0}} - u_y\big|_{\mathbf{0}}u_{yy}\big|_{\mathbf{0}}\right)h^3 + \mathcal{O}(\rho^4),\\
I_0 &= B_1 + \mathcal{O}(\rho^4),
\end{aligned}
$$

where $B_1 = (u_x^2\big|_{\mathbf{0}} + u_y^2\big|_{\mathbf{0}})h^2$. With easy computations, we obtain $\theta(\hat{\tau}_3) = 4$ with

$$
(21) \qquad \hat{\tau}_3 = |tI_{NE}^{(1)} + (u-t)I_{NW}^{(1)} + (u-t)I_{SE}^{(1)} + tI_{SW}^{(1)} - 2uI_0^{(2)}| \quad \forall t, u \in \mathbb{R}.
$$

No choices for the coefficients can delete the 11 coefficients of order ρ^4.

Finally, we point out that also in two dimensions we obtain, for the possible choices of ϵ, the same results as in CWENOZ3 in one dimension and reported in Table 2.

4. Numerical experiments. Here we present several tests in order to assess the performance of the schemes proposed in this work. In particular, we concentrate on those for which a novel definition of $\hat{\tau}$ has been proposed, namely the one-dimensional reconstructions CWENOZ3 and CWENOZ5 and the two-dimensional CWENOZ3.

First, in section 4.1 we test the accuracy and nonoscillatory properties of the novel CWENOZ reconstructions. Next, in section 4.2 we consider one-dimensional test problems and compare the CWENO reconstruction of [14] with the CWENOZ schemes. Finally, in section 4.3 we consider two-dimensional test problems based on the system of Euler equations for gas dynamics.

For the numerical solution, we apply schemes based on the local Lax–Friedrichs flux, with spatial reconstructions of orders 3 and 5 and the classical third order strong stability preserving Runge–Kutta scheme with three stages [22] and the fifth order Runge–Kutta scheme with six stages [8, sect. 3.2.5] for the time integration. The Butcher tableaux of the Runge–Kutta schemes are explicitly given in section SM3. All the simulations are run with a CFL of 0.45. All CWENO and CWENOZ reconstructions employ a central optimal weight $d_0 = \tfrac{3}{4}$ and set the d_k for $k \geq 1$ as in [14].

All one-dimensional tests were performed with the open source software `claw1dArena` [35].

4.1. Accuracy of the reconstructions. For the accuracy tests, we consider the following functions and critical points:

n_{cp}	function	x_{crit}
0	$u_0(x) = e^{-x^2}$	0.2
1	$u_1(x) = \sin(\pi x - \sin(\pi x)/\pi)$	0.596683186911209
2	$u_2(x) = 1.0 + \sin^3(\pi x)$	0.0
3	$u_3(x) = \cos^4(\pi x)$	0.2

Obviously, for $n_{cp} = 0$, $x_{\text{crit}} = 0.2$ is an evaluation point rather than a critical point. We compute the reconstruction polynomial for the cell containing the critical point, with cell averages initialized with a Gaussian quadrature rule of higher order than the expected order of accuracy. For these tests, quadruple precision was used.
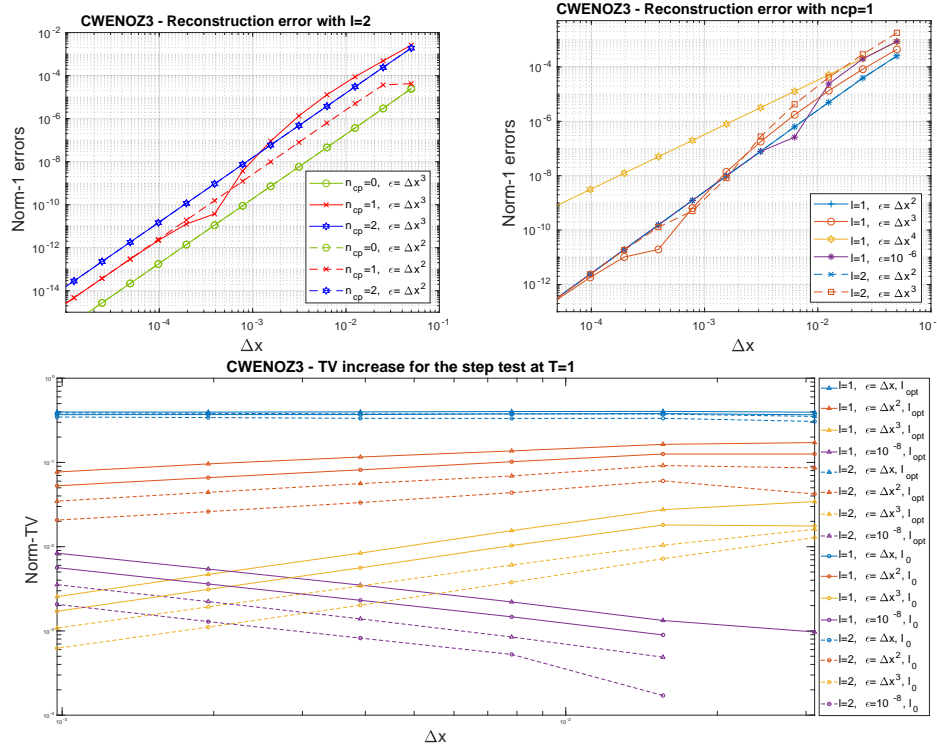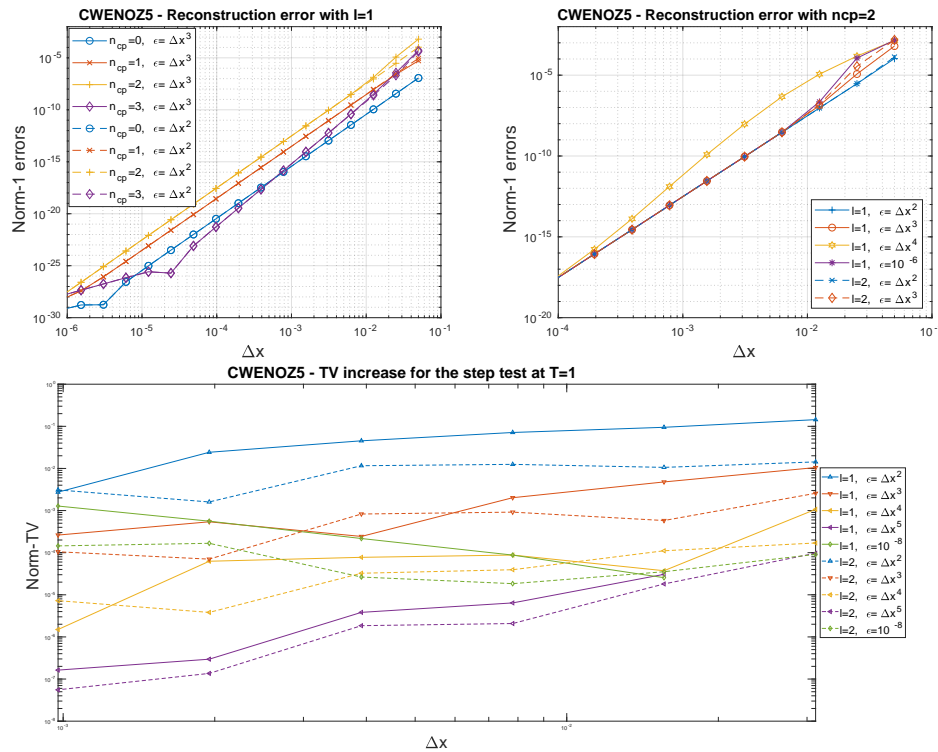
FIG. 1. *Results with the* CWENOZ3 *reconstruction. Top left: reconstruction error in a cell with* $n_{cp} = 0, 1, 2$, *using* $\ell = 1$. *Top right: reconstruction error in a cell with* $n_{cp} = 1$. *Bottom: total variation increase for the linear transport of a step (if a total variation decrease was observed, no data is reported).*

CWENOZ3. In Figure 1 we report on numerical experiments with the CWENOZ3 reconstruction. The top-left panel compares the reconstruction errors in a cell containing a critical point of order from 0 to 2, using $\ell = 2$ and $I_0 = I[P_{\mathsf{opt}}]$. The results indicate that the most difficult case is the presence of a critical point of order 1, which is further investigated in the top-right panel. For $\epsilon = \Delta x^4$ the reconstruction error does not decay with the correct order, showing that the bound of Theorem 24 is sharp. Also, for $\epsilon = \Delta x^3$, which is just within the bounds of Theorem 24, order 3 is indeed reached, but only for very small grids. These results are in agreement with those of Table 1. A similar irregular convergence history is observed when a fixed value of $\epsilon = 10^{-6}$ is employed. Finally, using $\ell = 1$ instead of $\ell = 2$ yields lower reconstruction errors (top right) and, on the contrary, defining $I_0 = I[P_0]$ yields slightly larger errors.

The bottom panel of Figure 1 analyzes the discontinuous case. A double step, namely $u(x, 0) = \chi_{[1/4, 3/4]}(x)$, was evolved with $u_t + u_x = 0$ in the domain $[0, 1]$ with periodic boundary conditions until $t = 1$. The increase in total variation at final time was studied as a measure of the spurious oscillations produced by the numerical scheme. Using a fixed value for ϵ yields a diminution of the total variation on very coarse grids (missing data in the plot), but an increase on smaller ones, leading to a non-TVD (Total Variation Diminishing) scheme asymptotically; the transition between the regimes happens at a grid size depending on the chosen value for ϵ. All choices $\hat{m} = 1, 2, 3$ lead to TVB (Total Variation Bounded) schemes, with $\hat{m} = 2, 3$

FIG. 2. *Results with the* CWENOZ5 *reconstruction. Top left: reconstruction error in a cell with* $n_{cp} = 0, 1, 2, 3$. *Top right: reconstruction error in a cell with* $n_{cp} = 2$. *Bottom: total variation increase for the linear transport of a step (if a total variation decrease was observed, no data is reported).*

also guaranteeing a diminution of the increase of the total variation when the grid size is reduced. Here the parameter ℓ and the choice of I_0 act opposite of the case of regular data: a smaller total variation error is obtained for larger values of ℓ and using $I_0 = I[P_0]$ instead of $I_0 = I[P_{\mathsf{opt}}]$.

In summary, unfortunately it is hard to indicate a parameter set that will perform optimally in all circumstances: $\hat{m} = 2$ to have good convergence rates on coarse grids for smooth data, together with $\ell = 2$ and $I_0 = I[P_0]$ to better control the total variation on discontinuous ones, seems the best overall choice, but better results can surely be obtained by fine-tuning the reconstruction parameters in specific situations.

CWENOZ5. In Figure 2 we report on numerical experiments with the CWENOZ5 reconstruction. The top-left panel compares the errors in a cell containing a critical point of order from 0 to 3, and the top-right panel investigates more carefully the more difficult situation, which is $n_{cp} = 2$. Apart from the choice $\epsilon = \Delta x^5$, which is just within the bounds of Theorem 24, order 5 is already reached on very coarse grids. Also the fixed choice $\epsilon = 10^{-6}$ leads to uneven convergence rates on coarse grids. In general, the parameter ℓ does not significantly influence the errors.

The bottom panel analyzes the discontinuous case. Similarly to the previous case, a fixed value of ϵ leads to an asymptotically non-TVB scheme. Also, the larger $\hat{m}$, the lower the total variation error and the higher the rate at which the total variation increase is reduced when refining the grid. Here too, using $\ell = 1$ reduces the
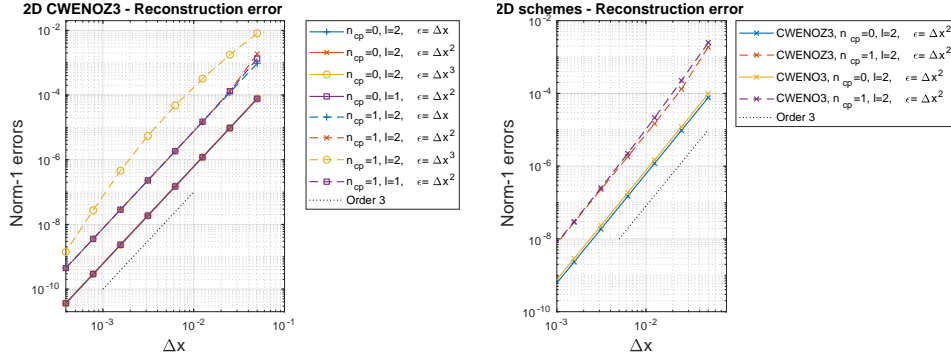
FIG. 3. *Reconstruction errors for the* CWENOZ3 *reconstruction in two dimensions (left panel) and comparison with the* CWENO *reconstruction in two dimensions (right panel).*

spurious oscillations (bottom panel) and the same happens when defining $I_0 = I[P_0]$ (not shown). However, due to the much smaller absolute values of the total variation increase (compare the vertical scale with that in Figure 1), we expect that spurious oscillations will be very small with any parameter set for CWENOZ5.

To summarize, we suggest employing $\hat{m} = 3$ or $\hat{m} = 4$ for CWENOZ5. Since ℓ does not play a major role, we suggest taking $\ell = 1$, which is computationally cheaper.

CWENOZ3 *in two dimensions.* Figure 3 shows the behavior of the CWENOZ3 reconstruction in two space dimensions. In particular, in the left panel one can see that the parameters ℓ and $\hat{m}$ do not significantly influence the performance of CWENOZ3 in a region with $n_{cp} = 0$, but the performance is reduced on coarse grids for $\hat{m} = 3$ and $n_{cp} = 1$. The situation is quite similar to the one-dimensional case. The right panel shows that the reconstruction errors are smaller for CWENOZ3 than for CWENO. In what follows, $\ell = 2$ and $\hat{m} = 2$ are used in all tests.

4.2. Conservation laws in one space dimension. In order to distinguish them, here we name CWENOZDB the schemes using, as in [13], the weights of Borges et al. [5] and simply use CWENOZ for the schemes using the new and improved weights introduced in section 3.1, namely $\hat{\tau}_3$ of (19) and $\hat{\tau}_5$ of (20), with $t = 1$.

Here, the value of ϵ is chosen as $\epsilon \approx \Delta x^{\hat{m}}$ for all of the schemes. In view of the convergence analysis of the nonlinear weights in section 3.1 and of the results of section 4.1, we consider the following choices.

For CWENOZ3 we show results for $\hat{m} = 2, 3$, $\ell = 1, 2$, and $I_0 = I[P_{\mathsf{opt}}]$ or $I_0 = I[P_0]$, showing that the best parameter set depends on the problem setting. Unless otherwise stated, the results are shown for $I_0 = I[P_{\mathsf{opt}}]$. For the CWENOZ5 scheme, we have tested $\hat{m} = 3, 4$, $\ell = 1, 2$, and both choices of I_0, but the schemes are almost insensitive to the parameters. Unless otherwise stated, the results are shown for $\hat{m} = 3$, $\ell = 1$, and $I_0 = I[P_{\mathsf{opt}}]$. Finally, for the CWENO and CWENOZDB schemes, we report the results with the settings of the papers [13, 14, 34], namely $\hat{m} = 2$, $\ell = 2$, and $I_0 = I[P_0]$.

Linear transport of smooth data. We solve the linear scalar conservation law

$$(22) \qquad\qquad u_t + u_x = 0$$

TABLE 3
The accuracy for the linear transport test of the high frequency smooth data (24) *with schemes of orders* 3 *and* 5.

cells	CWENO error	rate	CWENOZDB error	rate	CWENOZ3 ($\ell = 2$, $\hat{m} = 2$) error	rate	CWENO error	rate	CWENOZDB error	rate	CWENOZ5 ($\ell = 1$, $\hat{m} = 3$) error	rate
100	1.23e-01	-	1.22e-01	-	1.22e-01	-	1.16e-01	-	1.05e-01	-	9.53e-02	-
200	1.17e-01	0.06	1.14e-01	0.10	1.12e-01	0.12	1.43e-02	3.03	6.02e-03	4.11	6.00e-03	4.00
400	7.21e-02	0.70	5.23e-02	1.12	4.32e-02	1.38	6.08e-04	4.55	1.92e-04	4.97	1.93e-04	4.96
800	1.77e-02	2.03	1.08e-02	2.28	7.45e-03	2.54	2.16e-05	4.82	6.02e-06	5.00	6.03e-06	5.00
1600	4.43e-03	2.00	1.69e-03	2.68	8.95e-04	3.06	7.51e-07	4.85	1.88e-07	5.00	1.88e-07	5.00
3200	7.93e-04	2.45	2.03e-04	3.05	9.18e-05	3.28	2.73e-08	4.78	5.89e-09	5.00	5.89e-09	5.00

on the periodic domain $x \in [-0.5, 0.5]$ and up to final time $T = 1$. As an initial condition we consider the low frequency sinusoidal profile

$$(23) \qquad u_0(x) = \sin(2\pi x)$$

and the high frequency profile

$$(24) \qquad u_0(x) = \sin(2\pi x) + \sin(30\pi x) \exp(-80x^2).$$

The goal of this test is to numerically verify the convergence properties of the schemes.

For the low frequency datum (23), the 1-norm errors and the convergence rates as functions of increasing numbers of cells for the schemes of orders 3 and 5 are reported in section SM4.1. On this numerical test, the CWENOZ scheme and the CWENOZDB scheme have comparable errors and are always more accurate than the CWENO scheme. For the CWENOZ scheme of order 3 we do not see particular advantages in using different combinations of $\hat{m} = 2, 3$ and $\ell = 1, 2$. The best choice is given by $\ell = 2$ and $\hat{m} = 2$, for which we observe smaller errors than CWENOZDB on coarser grids.

Table 3 reports the data for the linear transport of the high frequency datum (24). Also in this case the errors of the CWENOZ5 are not strongly influenced by the choice of the parameters ℓ and $\hat{m}$. Moreover, the CWENOZ5 and CWENOZDB schemes provide the same results, showing improvement with respect to CWENO. On the other hand, CWENOZ3 is more sensible to the choice of the parameters ℓ and $\hat{m}$ as seen in Figure 4, where we compare $\ell = 1, 2$ and $\hat{m} = 2, 3$. We observe that, on this smooth problem, taking $\ell = 2$ and $\hat{m} = 2$ helps the scheme to reach the theoretical order of convergence also on coarser grids, according to analysis and tests in sections 3.1 and 4.1. All of the methods reach the expected theoretical order of convergence, but we point out that the error of the CWENOZ3 scheme with this optimal choice of the parameters (in particular for $\ell = 1$ and $\hat{m} = 2$) is more than half an order of magnitude better than the accuracy of CWENOZDB and CWENO. This also demonstrates that the new and improved weights computed in section 3.1 for one-dimensional reconstructions improve the quality of the solution.

Linear transport of a nonsmooth datum: The Jiang–Shu test. This problem, designed by Jiang and Shu in [27], is used in order to investigate the properties of a scheme to transport different shapes with minimal dissipation and dispersion effects. We again consider the linear scalar conservation law (22) but on the periodic domain $x \in [-1, 1]$. The initial datum, which is given by equation (SM6) in section SM4.2, is a combination of smooth and nonsmooth shapes. More precisely, from the left side to the right side of the domain, we have a Gaussian, a square wave, a sharp triangle wave, and a half ellipse. The final time is set to $T = 8$.
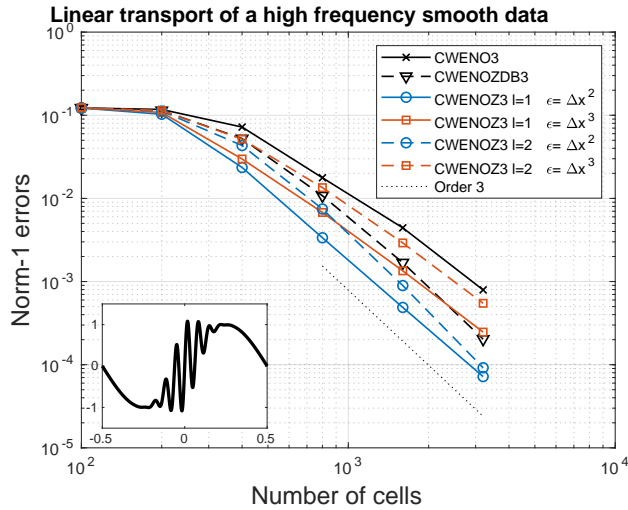
FIG. 4. *Convergence plot of the* CWENO, CWENOZDB, *and* CWENOZ *schemes of order* 3 *for the high frequency datum* (24).

The top panel of Figure 5 shows the numerical solution of the Jiang–Shu test problem computed with the CWENO, CWENOZDB3, and CWENOZ3 schemes on 400 cells. For the CWENOZ3 schemes, we compare the solutions for the parameters $\hat{m} = 2, 3$ with fixed $\ell = 2$ since the choice $\ell = 1$ leads to more oscillatory schemes around the discontinuities of the square wave (see section 4.1). Moreover, for the same sets of parameters, we also consider the CWENOZ3 schemes with the indicator $I_0 = I[P_0]$.

In the bottom panels of Figure 5 we focus on the top parts of the Gaussian wave and of the square waves since they give information on the behavior of the schemes on smooth and nonsmooth zones of the solution. In the case of a smooth profile, we observe that CWENOZ3 and CWENOZDB are less diffusive than CWENO. In particular, the CWENOZ3 schemes with $\hat{m} = 2$ provide a better approximation of the top of the Gaussian wave. We do not observe a significant difference when using $I_0 = I[P_0]$. The situation for the top of the square wave (bottom right panel of Figure 5) is more complex. The CWENOZ3 scheme with $\hat{m} = 2$ and the CWENOZDB scheme seem to be more oscillatory than CWENO. However, the choice of the parameter $\hat{m} = 3$ for the CWENOZ3 scheme allows us to dampen the spurious oscillations across the discontinuities, and it also provides a less diffusive approximation than CWENO. In general, we also observe that using $I_0 = I[P_0]$ for the CWENOZ3 schemes mitigates the amplitude of the oscillations.

Figure 6 shows the numerical solution computed with the CWENO, CWENOZDB, and CWENOZ5 schemes on 400 cells. In this case, we consider only the parameters $\ell = 1$ and $\hat{m} = 3$ for the CWENOZ5 scheme. All schemes accurately reproduce the solution at final time with significant improvement with respect to the schemes of order 3. However, some zones, shown in the bottom panels of Figure 6, deserve more attention since they highlight the advantages of CWENOZ5. We show the top part of the square wave (left panel) and the bottom part of the half ellipse (right panel). We note that the CWENO scheme exhibits undershoots. On the contrary, the CWENOZDB and CWENOZ5 schemes avoid the oscillations. In particular, the CWENOZ5 scheme has a slightly better resolution with less diffusivity close to the
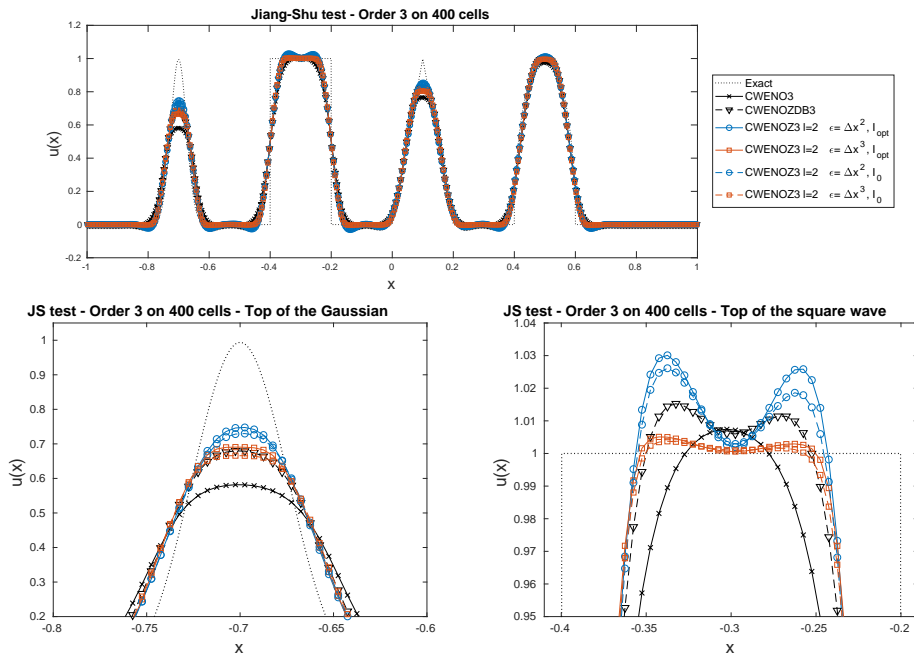
FIG. 5. *Top panel: numerical solution of the Jiang–Shu test problem* (SM6) *with schemes of order* 3 *and* 400 *cells. Bottom panels: top part of the Gaussian wave (left) and top part of the square wave (right).*

discontinuities, showing that the new weights designed in section 3.1 improve the accuracy.

One-dimensional Euler equations: The shock-acoustic interaction test. We consider the one-dimensional system of Euler equations for gas dynamics,

$$\partial_t \begin{pmatrix} \rho \\ \rho u \\ E \end{pmatrix} + \partial_x \begin{pmatrix} \rho u \\ \rho u^2 + p \\ u(E + p) \end{pmatrix} = 0,$$

where ρ, u, p, and E are the density, velocity, pressure, and energy per unit volume of an ideal gas, whose equation of state is $E = \frac{p}{\gamma - 1} + \frac{1}{2}\rho u^2$, where $\gamma = 1.4$.

In this test we simulate the interaction of a strong shock with an acoustic wave on the domain $x \in [-5, 5]$ with free-flow boundary conditions. The problem was introduced by Shu and Osher in [39] and is characterized by a Mach 3 shock wave interacting with a standing sinusoidal density wave. The solution, behind the main strong shock, develops a combination of smooth waves and small discontinuities. The initial condition is given in equation (SM7) of section SM4.3, and we run the problem up to the final time $T = 1.8$.

Figure 7 shows the numerical results computed with the CWENO, CWENOZDB3, and CWENOZ3 schemes on 800 cells. For the CWENOZ3 scheme, in view of the previous experiments, we consider $\ell = 2$ with $\hat{m} = 2, 3$. The bottom panels show the zoom-in of the solution in two regions of the computational domain. The reference solution (black dotted line) was generated using 8000 cells and the fifth order CWENO scheme. We observe that CWENOZ3, which employs the new and improved weights introduced in section 3.1, provides a better resolution, in particular with $\hat{m} = 2$, of
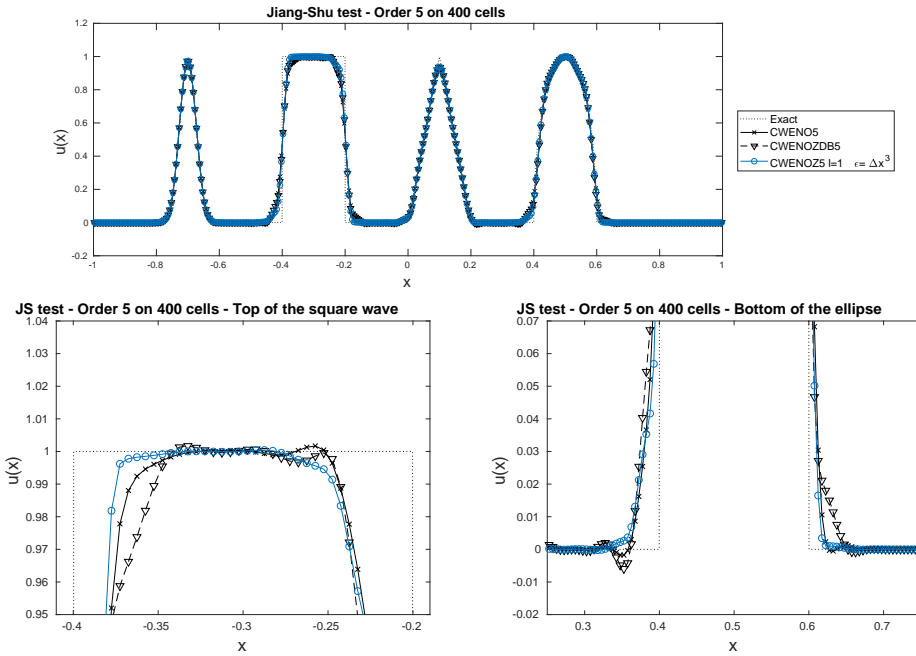
FIG. 6. *Top panel: numerical solution of the Jiang–Shu test problem* (SM6) *with schemes of order* 5 *and* 400 *cells. Bottom panels: top part of the square wave (left) and bottom part of the half ellipse (right).*

the turbulence region, which is characterized by the smooth high frequency solution behind the main shock (bottom right panel of Figure 7). No extra oscillations at discontinuity are observed: the main shock and the shocklets are approximated better by the new CWENOZ3 schemes, in particular with respect to CWENO, which is more diffusive. Moreover, note that, despite the fact that the kink at the shock is under-resolved by the grid, no oscillations arise with any of the schemes.

Summary of the one-dimensional tests. For CWENOZ5, $\ell = 1$ and $\hat{m} = 3$ with the standard choice $I_0 = I[P_{\mathsf{opt}}]$ performed well in all circumstances. Using $\hat{m} = 4$ would yield even smaller spurious oscillations close to discontinuities, but in any case, the dependence of CWENOZ5 on the choice of ℓ, $\hat{m}$, and I_0 proved to be weak.

On the other hand, CWENOZ3 exhibits a stronger dependence on the parameters. A sensible general choice is $\hat{m} = 2$, which yields lower errors on smooth flows, coupled with $\ell = 2$ and $I_0 = I[P_0]$, which reduce the oscillations around discontinuities. However, we point out that the case when $\hat{m} = 3$ and $\ell = 1$ produces significantly fewer oscillations than the previous case and is comparable with CWENOZDB3 in smooth parts: it could be a valid choice for problems where controlling spurious oscillations is more important than resolving the smooth parts on coarse grids.

4.3. Two space dimensions. In the following paragraphs, we consider test problems based on the two-dimensional system of Euler equations for gas dynamics

$$\partial_t \begin{pmatrix} \rho \\ \rho u \\ \rho v \\ E \end{pmatrix} + \partial_x \begin{pmatrix} \rho u \\ \rho u^2 + p \\ \rho uv \\ u(E+p) \end{pmatrix} + \partial_y \begin{pmatrix} \rho v \\ \rho uv \\ \rho v^2 + p \\ v(E+p) \end{pmatrix} = 0,$$
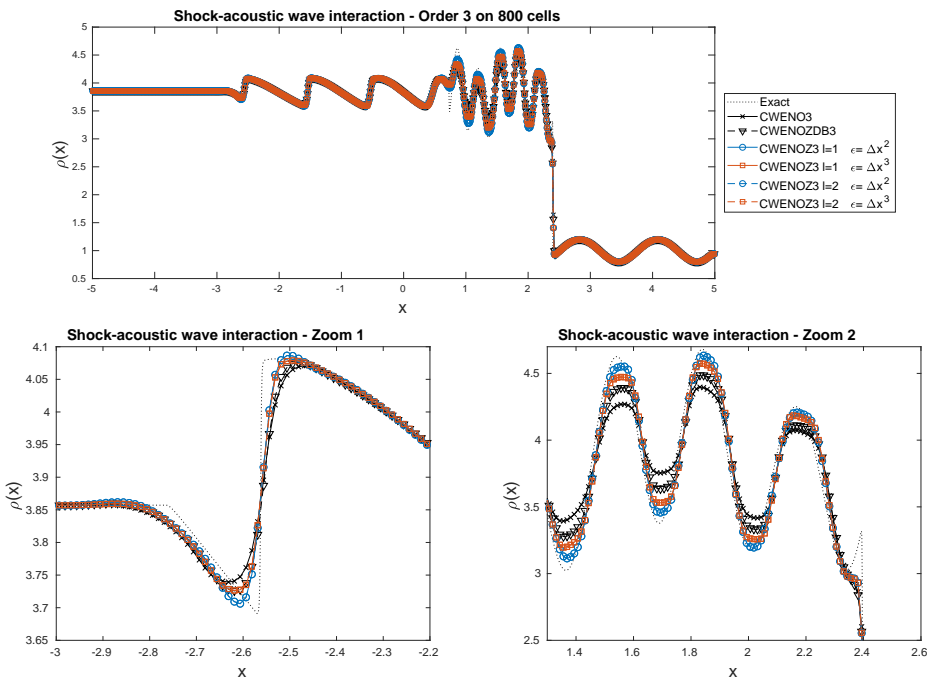
FIG. 7. *Numerical solution and zoom-in on two regions of the shock-acoustic wave interaction problem with schemes of order* 3 *on* 800 *cells.*

where ρ, u, v, p, and E are the density, the velocity in the x and y directions, the pressure, and the energy per unit mass. The thermodynamic closure is given by the equation of state $E = \frac{p}{\gamma-1} + \frac{1}{2}\rho(u^2 + v^2)$, where we take $\gamma = 1.4$.

We consider three schemes that do not rely on dimensional splitting. We make use of the two-dimensional reconstruction procedure CWENO of [34], the novel CWENOZ3 that employs the definition of $\hat{\tau}$ given in (21) with $t = 1, u = 2$, that is,

$$(25) \qquad \hat{\tau}_3 = |I_{NE}^{(1)} + I_{NW}^{(1)} + I_{SE}^{(1)} + I_{SW}^{(1)} - 4I_0^{(2)}|,$$

and we also consider the alternative definition with $t = 1, u = 0$ that leads to

$$(26) \qquad \hat{\tau}_{3B} = |I_{NE}^{(1)} - I_{NW}^{(1)} - I_{SE}^{(1)} + I_{SW}^{(1)}|,$$

giving it the name CWENOZ3(b). This latter does not use the indicator of the optimal polynomial in the definition of $\hat{\tau}$. After the one-dimensional results, we consider $\ell = 2$, $\hat{m} = 2$, and $I_0 = I[P_{\mathsf{opt}}]$.

For the computation of the numerical fluxes across the cell faces, 2-point Gauss formulas are employed, and their nodes dictate the positions where the point-value reconstructions are computed, totalling eight reconstructed values per cell. The rest of the numerical scheme is the straightforward generalization of the one-dimensional scheme. The implementation was carried on with the help of the PETSc libraries to handle parallelism, and the simulations were run on a 24-core node of the OCCAM cluster of the C3S center of the Università di Torino (https://c3s.unito.it).

Two-dimensional convergence test: The isentropic vortex. This problem was introduced by Shu in [37] and is commonly used for testing the order of accuracy of a

TABLE 4
The accuracy for the isentropic vortex test with schemes of order 3.

	Density variable						Energy variable					
	CWENO3		CWENOZ3		CWENOZ3(b)		CWENO3		CWENOZ3		CWENOZ3(b)	
cells	error	rate	error	rate	error	rate	error	rate	error	rate	error	rate
50	2.97e-01	-	3.28e-01	-	3.43e-01	-	1.93e-00	-	1.83e-00	-	1.83e-00	-
100	6.01e-02	2.31	6.41e-02	2.36	6.43e-02	2.41	3.23e-01	2.58	3.08e-01	2.57	3.08e-01	2.57
200	9.15e-03	2.72	9.03e-03	2.83	9.04e-03	2.83	4.46e-02	2.86	4.24e-02	2.86	4.24e-02	2.86
400	1.25e-03	2.87	1.15e-03	2.97	1.15e-03	2.97	5.73e-03	2.96	5.39e-03	2.97	5.39e-03	2.97
800	1.61e-04	2.96	1.44e-04	3.00	1.44e-04	3.00	7.28e-04	2.98	6.82e-04	2.98	6.82e-04	2.98
1600	2.02e-05	2.99	1.80e-05	3.00	1.80e-05	3.00	9.70e-05	2.91	9.12e-05	2.90	9.12e-05	2.90

numerical scheme since an exact, smooth, and analytic solution is known at all times. The initial condition is given in section SM5.1 and it is characterized by a uniform ambient flow with constant temperature, density, velocity, and pressure onto which an isentropic perturbation is added. The numerical tests are performed on the computational domain $[-5,5] \times [-5,5]$ with periodic boundary conditions. As a result of isentropy, the exact solution of this problem is simply the advection of the initial condition with velocity (u_∞, v_∞). At the final time $T = 10$ the vortex is thus back in its original position. Since the solution is smooth, it should be computed with optimal high accuracy, and the limiting/stabilization procedure employed in the scheme should not have any effect.

In Table 4 we show the errors and the convergence rates in density and in total energy for the isentropic vortex test with the two-dimensional schemes of order 3. We observe that all schemes reach the theoretical order of convergence. Both CWENOZ reconstructions yield lower errors and better convergence rates than CWENO, in particular for the energy variable. Both CWENOZ3 schemes provide similar results.

However, in the tests involving strong shocks, we have observed that the indicator employed in CWENOZ3(b), which does not take into account the central interpolating polynomial in the expression for $\hat{\tau}$, may lead to a breakdown of the simulations, in particular in the forward-facing step and in the double Mach reflection problems. For this reason, only the results for CWENO and CWENOZ3 are presented in the final part of the paper.

The forward-facing step problem. This problem was proposed by Emery [20] and Woodward and Colella [41]. It is characterized by a Mach 3 flow entering from the left in a wind tunnel that has a reduction of size due to a step, which opposes the direction of the flow, emanating shock waves that later are reflected back by the top wall (see section SM5.2). The challenges of this problem are the stability in the initial boundary layer on the step and of the flow around the corner, and the emergence of shock waves bouncing off the walls and interacting among themselves. In particular, the wave emerging from the triple point in the upper region is Rayleigh–Taylor unstable, but diffusive numerical schemes often smooth out the instability.

First, we compare the solutions computed on a grid of 1920×640 cells (1M degrees of freedom) by the CWENO and CWENOZ schemes of order 3. We point out that for both schemes, no special treatment was needed at the corner of the step which is the center of a rarefaction fan.

In Figure 8 we plot the solutions at time $t = 2.6$, when the contact discontinuity that emerges from the triple point has just formed. Here it is evident that the CWENOZ3 scheme can correctly compute the Rayleigh–Taylor instability of the contact that appears almost stable with the CWENO3 scheme at this resolution. At later times, the instability diffuses out also with the CWENOZ3 scheme.
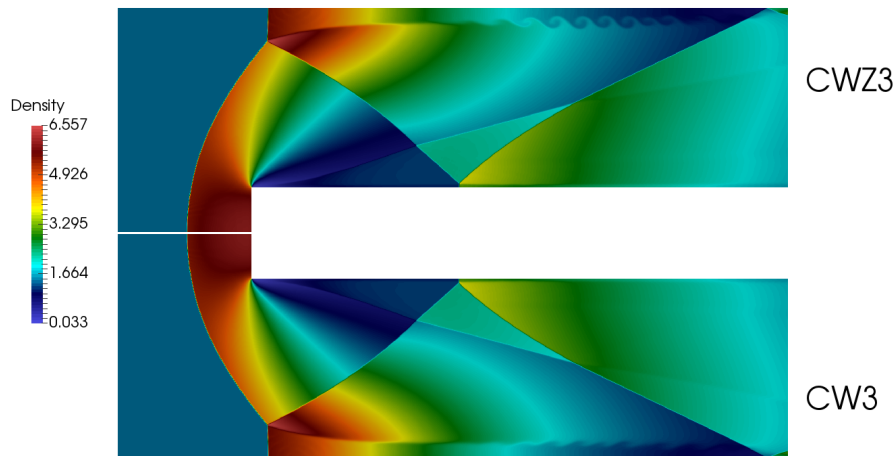
FIG. 8. *Numerical solution of the forward-facing step problem at time* $t = 2.4$ *with the* CWENOZ *(top) and* CWENO *(bottom) schemes of order* 3.

The plot of the solution at final time $T = 4$ using an even finer grid (3480×1280 cells) can be found in section SM5.2. It is evident that the curly instability patterns around the contact are maintained by the CWENOZ3 scheme, while the CWENO3 scheme has completely diffused them even on this finer grid with 4M degrees of freedom.

Double Mach reflection problem. The double Mach reflection problem of a strong shock was originally proposed by Woodward and Colella [41]. The problem is characterized by a Mach 10 shock, which is incident on a ramp. The initial condition is discussed in detail in section SM5.3. As the shock moves, it hits the ramp, and a complex shock reflection structure forms. This test is challenging due to the contemporaneous presence of strong waves, very weak ones, and complex smooth features in the so-called recirculation zone.

The problem was run on a mesh of 2560×800 cells (2M degrees of freedom) and on a finer mesh of 5120 cells (8M degrees of freedom) until $T = 0.2$. The exact solution of this problem is not available, but it is known that the discontinuity produces Kelvin–Helmholtz instabilities when high-resolution and sufficiently nondissipative schemes are employed for the simulation. The solutions in the entire domain are included in section SM5.3. Figure 9 here shows a zoom-in of the solutions in the recirculation zone.

We observe that the CWENO scheme cannot reproduce the Kelvin–Helmholtz phenomenon on the coarser grid, while the CWENOZ3 shows the instabilities across the moving stem. On the finer grid, both schemes show the instability of the solution. This proves that the CWENOZ3 scheme, with the new and improved weights proposed in section 3.2, has better accuracy than the classical version CWENO.

Shock-bubble interaction. Here we consider the challenging problem in which a right-moving shock impinges on a standing bubble of gas at lower density; see [9, 34] and section SM5.4 for details.

For this test we present the comparison of the solutions computed with CWENO and CWENOZ3 at different times and different resolutions. The more remarkable
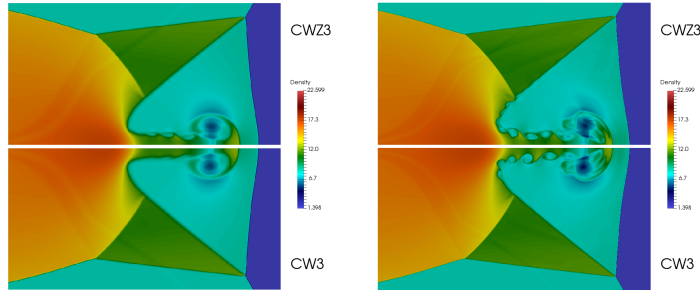
FIG. 9. *Numerical solution of the double Mach reflection problem with the* CWENOZ *(top) and* CWENO *(bottom) schemes of order* 3. *Left: grid of* 2560×800 *cells. Right: grid of* 5120×1600 *cells.*
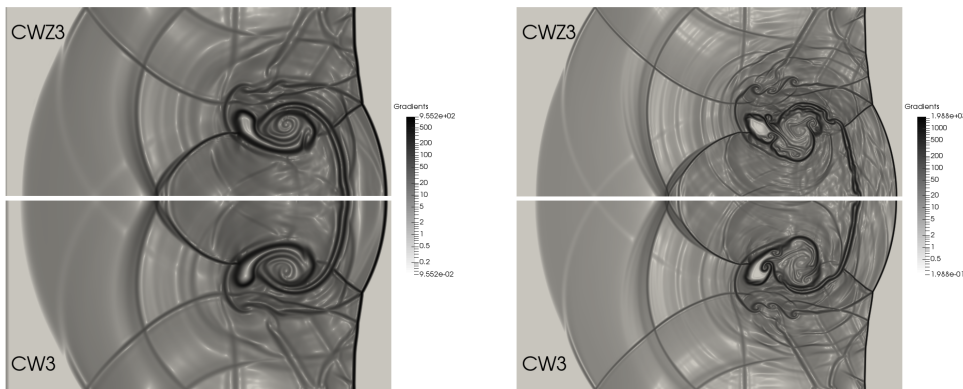

FIG. 10. *Numerical solution of the shock-bubble interaction problem at* $t = 0.32$ *with the* CWENOZ *and* CWENO *schemes of order* 3 *on a grid of* 1360×400 *cells (top) and* 2720×800 *(bottom).*

differences can be appreciated in the Schlieren plots; see Figures 10 and 11 for the zoom-ins and section SM5.4 for the complete domain. When the shock impinges on the low-density bubble, it pushes forward and deforms it while being refracted through it. The refracted shock then bounces back towards the bubble, creating a very complex interaction pattern. Moreover, the bubble is known to be unstable, and the CWENOZ3 is already able to show its instability on the coarser grid, where small differences start to appear, while on the finer grid it computes a much more complex breaking and interaction pattern due to its enhanced resolution.

5. Conclusions. In this paper we analyzed the optimal definition of the global smoothness indicator employed in the computation of the WENOZ-style nonlinear weights in the setting of central WENO reconstructions. The analysis is performed in multidimensions, avoiding the use of dimensional splitting, so that it is generalizable to grid setups that are less regular than the ones considered here.

To this end, in particular we proved asymptotic expansions of the Jiang–Shu smoothness indicators in $\mathbb{R}^n$ and derived a general result on the consistency order of CWENO and CWENOZ reconstructions. Next, we considered again the CWENOZ reconstructions introduced in [13] and, with the help of the above-mentioned results, defined the optimal $\hat{\tau}$ indicator for this setup. Finally, we introduced a third order
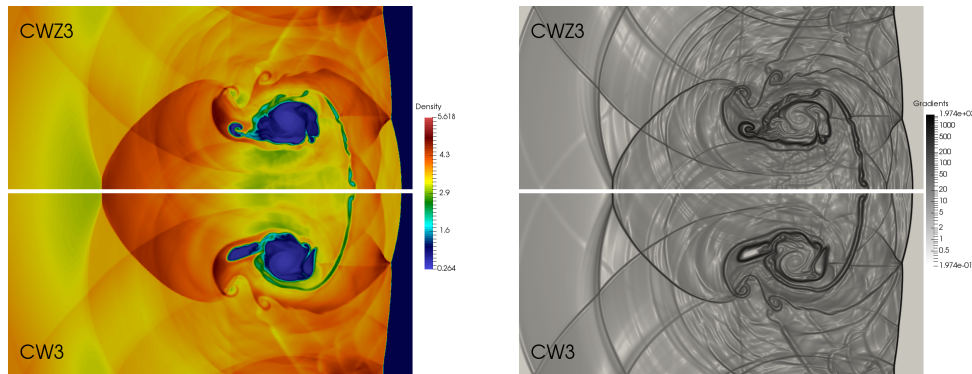
FIG. 11. *Numerical solution of the shock-bubble interaction problem at final time* $T = 0.4$ *with the* CWENOZ *and* CWENO *schemes of order* 3 *on a grid of* 2720×800.

CWENOZ reconstruction in two space dimensions that is based on the same stencils of the CWENO reconstruction of [34, 12]. Numerous one- and two-dimensional numerical tests confirmed the improved resolution of the new schemes.

The optimal global smoothness indicators defined for the reconstructions of this paper are constructed on the basis of results on the asymptotic expansions of the Jiang–Shu indicators that are quite general. We think these results may prove very useful in the design of future CWENOZ reconstructions based on different choices of meshes, stencils, and polynomial degrees. In particular, Corollary 22 provides a general result on the definition of the global smoothness indicator τ for CWENOZ schemes that is valid on any grid setup.

REFERENCES

[1] F. ACKER, R. B. DE R. BORGES, AND B. COSTA, *An improved WENO-Z scheme*, J. Comput. Phys., 313 (2016), pp. 726–753, https://doi.org/10.1016/j.jcp.2016.01.038.

[2] F. ARÀNDIGA, A. BAEZA, A. M. BELDA, AND P. MULET, *Analysis of WENO schemes for full and global accuracy*, SIAM J. Numer. Anal., 49 (2011), pp. 893–915, https://doi.org/10.1137/100791579.

[3] D. S. BALSARA, S. GARAIN, AND C.-W. SHU, *An efficient class of WENO schemes with adaptive order*, J. Comput. Phys., 326 (2016), pp. 780–804, https://doi.org/10.1016/j.jcp.2016.09.009.

[4] D. S. BALSARA, T. RUMPF, M. DUMBSER, AND C.-D. MUNZ, *Efficient, high accuracy ADER-WENO schemes for hydrodynamics and divergence-free magnetohydrodynamics*, J. Comput. Phys., 228 (2009), pp. 2480–2516, https://doi.org/10.1016/j.jcp.2008.12.003.

[5] R. BORGES, M. CARMONA, B. COSTA, AND W. S. DON, *An improved weighted essentially non-oscillatory scheme for hyperbolic conservation laws*, J. Comput. Phys., 227 (2008), pp. 3191–3211.

[6] S. BOSCARINO, G. RUSSO, AND M. SEMPLICE, *High order finite volume schemes for balance laws with stiff relaxation*, Comput. Fluids, 169 (2018), pp. 155–168, https://doi.org/10.1016/j.compfluid.2017.10.009.

[7] W. BOSCHERI, M. SEMPLICE, AND M. DUMBSER, *Central WENO subcell finite volume limiters for ADER discontinuous Galerkin schemes on fixed and moving unstructured meshes*, Commun. Comput. Phys., 25 (2019), pp. 311–346, https://doi.org/10.4208/cicp.OA-2018-0069.

[8] J. C. Butcher, *Numerical Methods for Ordinary Differential Equations*, 2nd ed., Wiley, 2008.

[9] M. Cada and M. Torrilhon, *Compact third order limiter functions for finite volume methods*, J. Comput. Phys., 228 (2009), pp. 4118–4145.

[10] G. Capdeville, *A central WENO scheme for solving hyperbolic conservation laws on non-uniform meshes*, J. Comput. Phys., 227 (2008), pp. 2977–3014.

[11] M. Castro, B. Costa, and W. S. Don, *High order weighted essentially non-oscillatory WENO-Z schemes for hyperbolic conservation laws*, J. Comput. Phys., 230 (2011), pp. 1766–1792, https://doi.org/10.1016/j.jcp.2010.11.028.

[12] M. J. Castro-Dìaz and M. Semplice, *Third and fourth order well-balanced schemes for the shallow water equations based on the CWENO reconstruction*, Int. J. Numer. Methods Fluids, 89 (2019), pp. 304–325, https://doi.org/10.1002/fld.4700.

[13] I. Cravero, G. Puppo, M. Semplice, and G. Visconti, *Cool WENO schemes*, Comput. & Fluids, 169 (2018), pp. 71–86, https://doi.org/10.1016/j.compfluid.2017.07.022.

[14] I. Cravero, G. Puppo, M. Semplice, and G. Visconti, *CWENO: Uniformly accurate reconstructions for balance laws*, Math. Comp., 87 (2018), pp. 1689–1719, https://doi.org/10.1090/mcom/3273.

[15] I. Cravero and M. Semplice, *On the accuracy of WENO and CWENO reconstructions of third order on nonuniform meshes*, J. Sci. Comput., 67 (2016), pp. 1219–1246, https://doi.org/10.1007/s10915-015-0123-3.

[16] W.-S. Don and R. Borges, *Accuracy of the weighted essentially non-oscillatory conservative finite difference schemes*, J. Comput. Phys., 250 (2013), pp. 347–372.

[17] M. Dumbser, D. S. Balsara, E. F. Toro, and C.-D. Munz, *A unified framework for the construction of one-step finite volume and discontinuous Galerkin schemes on unstructured meshes*, J. Comput. Phys., 227 (2008), pp. 8209–8253, https://doi.org/10.1016/j.jcp.2008.05.025.

[18] M. Dumbser, W. Boscheri, M. Semplice, and G. Russo, *Central weighted ENO schemes for hyperbolic conservation laws on fixed and moving unstructured meshes*, SIAM J. Sci. Comput., 39 (2017), pp. A2564–A2591, https://doi.org/10.1137/17M1111036.

[19] M. Dumbser, M. Kaeser, V. A. Titarev, and E. F. Toro, *Quadrature-free non-oscillatory finite volume schemes on unstructured meshes for nonlinear hyperbolic systems*, J. Comput. Phys., 226 (2007), pp. 204–243.

[20] A. F. Emery, *An evaluation of several differencing methods for inviscid fluid flow problems*, J. Comput. Phys., 2 (1968), pp. 306–331.

[21] J. M. Gallardo, S. Ortega, M. de la Asunción, and J. M. Mantas, *Two-dimensional compact third-order polynomial reconstructions. Solving nonconservative hyperbolic systems using GPUs*, J. Sci. Comput., 48 (2011), pp. 141–163, https://doi.org/10.1007/s10915-011-9470-x.

[22] S. Gottlieb, C.-W. Shu, and E. Tadmor, *Strong stability-preserving high-order time discretization methods*, SIAM Rev., 43 (2001), pp. 89–112, https://doi.org/10.1137/S003614450036757X.

[23] A. Harten, B. Engquist, S. Osher, and S. R. Chakravarthy, *Uniformly high order accurate essentially non-oscillatory schemes*, J. Comput. Phys., 71 (1987), pp. 231–303.

[24] A. K. Henrick, T. D. Aslam, and J. M. Powers, *Mapped weighted essentially non-oscillatory schemes: Achieving optimal order near critical points*, J. Comput. Phys., 207 (2005), pp. 542–567.

[25] C. Hu and C.-W. Shu, *A high-order WENO finite difference scheme for the equations of ideal magnetohydrodynamics*, J. Comput. Phys., 150 (1999), pp. 561–594.

[26] C. Hu and C.-W. Shu, *Weighted essentially non-oscillatory schemes on triangular meshes*, J. Comput. Phys., 150 (1999), pp. 97–127, https://doi.org/10.1006/jcph.1998.6165.

[27] G.-S. Jiang and C.-W. Shu, *Efficient implementation of weighted ENO schemes*, J. Comput. Phys., 126 (1996), pp. 202–228.

[28] O. Kolb, *On the full and global accuracy of a compact third order WENO scheme*, SIAM J. Numer. Anal., 52 (2014), pp. 2335–2355, https://doi.org/10.1137/130947568.

[29] M. Lahooti and A. Pishevar, *A new fourth order central WENO method for 3D hyperbolic conservation laws*, Appl. Math. Comput., 218 (2012), pp. 10258–10270, https://doi.org/10.1016/j.amc.2012.04.003.

[30] D. Levy, G. Puppo, and G. Russo, *Central WENO schemes for hyperbolic systems of conservation laws*, M2AN Math. Model. Numer. Anal., 33 (1999), pp. 547–571, https://doi.org/10.1051/m2an:1999152.

[31] D. Levy, G. Puppo, and G. Russo, *Compact central WENO schemes for multidimensional conservation laws*, SIAM J. Sci. Comput., 22 (2000), pp. 656–672, https://doi.org/10.1137/S1064827599359461.

[32] D. Levy, G. Puppo, and G. Russo, *A third order central WENO scheme for* 2*D conservation laws*, Appl. Numer. Math., 33 (2000), pp. 415–421, https://doi.org/10.1016/S0168-9274(99)00108-7.

[33] J. Qiu and C.-W. Shu, *On the construction, comparison, and local characteristic decomposition for high-order central WENO schemes*, J. Comput. Phys., 183 (2002), pp. 187–209, https://doi.org/10.1006/jcph.2002.7191.

[34] M. Semplice, A. Coco, and G. Russo, *Adaptive mesh refinement for hyperbolic systems based on third-order compact WENO reconstruction*, J. Sci. Comput., 66 (2016), pp. 692–724, https://doi.org/10.1007/s10915-015-0038-z.

[35] M. Semplice and G. Visconti, *claw*1*dArena*, https://doi.org/10.5281/zenodo.2641724, 2019.

[36] J. Shi, C. Hu, and C.-W. Shu, *A technique of treating negative weights in WENO schemes*, J. Comput. Phys., 175 (2002), pp. 108–127.

[37] C.-W. Shu, *Essentially Non-Oscillatory and Weighted Essentially Non-Oscillatory Schemes for Hyperbolic Conservation Laws*, NASA/CR-97-206253 ICASE Report 97-65, 1997.

[38] C.-W. Shu, *High order weighted essentially nonoscillatory schemes for convection dominated problems*, SIAM Rev., 51 (2009), pp. 82–126, https://doi.org/10.1137/070679065.

[39] C.-W. Shu and S. Osher, *Efficient implementation of essentially non-oscillatory shock-capturing schemes* II, J. Comput. Phys., 83 (1989), pp. 32–78.

[40] P. Tsoutsanis, V. A. Titarev, and D. Drikakis, *WENO schemes on arbitrary mixed-element unstructured meshes in three space dimensions*, J. Comput. Phys., 230 (2011), pp. 1585–1601.

[41] P. Woodward and P. Colella, *The numerical simulation of two-dimensional fluid flow with strong shocks*, J. Comput. Phys., 54 (1984), pp. 115–173.

[42] X. Wu and Y. Zhao, *A high-resolution hybrid scheme for hyperbolic conservation laws*, Internat. J. Numer. Methods Fluids, 78 (2015), pp. 162–187, https://doi.org/10.1002/fld.4014.

[43] Y. H. Zahran, *An efficient WENO scheme for solving hyperbolic conservation laws*, Appl. Math. Comput., 212 (2009), pp. 37–50, https://doi.org/10.1016/j.amc.2009.01.085.

[44] Y. T. Zhang and C.-W. Shu, *Third order WENO scheme on three dimensional tetrahedral meshes*, Commun. Comput. Phys., 5 (2009), pp. 836–848.

[45] J. Zhu and J. Qiu, *A new type of finite volume WENO schemes for hyperbolic conservation laws*, J. Sci. Comput., 73 (2017), pp. 1338–1359, https://doi.org/10.1007/s10915-017-0486-8.

[46] J. Zhu and J. Qiu, *New finite volume weighted essentially nonoscillatory schemes on triangular meshes*, SIAM J. Sci. Comput., 40 (2018), pp. A903–A928, https://doi.org/10.1137/17M1112790.